STUDY OF X-PINCH PLASMA DYNAMICS USING A 40kA PULSED POWER PLASMA DEVICE

Nikolaos Ligopsihakis

Master thesis for the MSc program:
“Plasma Physics and Applications”

2019

Supervision committee:

1. Dr. Tatarakis Michael
2. Dr. Dimitriou Vasilis
3. Dr. Chatzakis Ioannis

Supervision committee:

1. Dr. Tatarakis Michael
2. Dr. Dimitriou Vasilis
3. Dr. Chatzakis Ioannis

Thesis examination committee:

1. Dr. Tatarakis Michael
2. Dr. Dimitriou Vasilis
3. Dr. Benis Manolis

Keywords

Plasma Physics
Plasma dynamics
Plasma density
Phase shift
Interferometry
Shawdography
Index of refraction
X-pinch
X-rays
Instabilities
Electron beam
Hotspot

Abstract

The X-pinch device may produce extreme plasma conditions able to offer the opportunity and the demanded conditions for studies on high-energy-density plasma and X-ray source for imaging. The experimental study of the X-pinch plasma dynamics for peak current of 40 kA and rise-time 50 ns is presented in this thesis. A Tungsten wire of 5 µm thickness was used as a target at the experiments performed. The main objectives of this research were to investigate the plasma jets dynamics, the X-ray emission and the time evolution of the plasma at the X point. Soft X-rays, in a range of ~8.3 to ~11 keV, emitted from the cross-point were observed, approximately at the peak current. Also, hard X-rays bursts, K lines, were observed from the minidiodes that were emerging.

Acknowledgements

First, I would like to thank the Director of the CPPL, Professor Michael Tatarakis who gave me the opportunity to participate in laboratory experiments in the field of Plasma Physics. My thanks are extended to Alexandros Skoulakis, member of the lab, for his excellent support, guidance and encouragement throughout my experiments.

I would like to thank Dr. Vasilis Dimitriou, Dr. Ioannis Fitilis and Dr. Evaggelos Kaselouris for their support and for providing me essential information for the experimental analysis procedure.

I would also like to special thanks Ioannis Chatzakis and Manolis Benis, members of my supervision and examination committee.

Finally, thanks to my fiancée, Theodora Koumoudeli, and my parents who without their support I could never completed this Thesis. I would like also to thank my postgraduate classmates in master of Plasma Physics and Applications for the beautiful moments and their support.

Table of Contents

List of Figures

Chapter 1

Chapter 2

Chapter 3

List of Tables

Chapter 1

Chapter 2

List of Abbreviations

Al	Aluminum
Cu	Copper
DPP	Discharge Produced Plasma
W	tungsten
Nd YAG	Neodymium-doped Yttrium Aluminum Garnet
SXR	Soft X-rays
HXR	Hard X-rays
O waves	Ordinary waves
X waves	Extra-ordinary waves
R waves	Right-hand and circularly polarized waves
L waves	Left-hand circularly polarized waves
PFL	Pulse Forming Line
PD	Photodiode
PMT	Photomultiplier
SF6	Sulfur hexafluoride
CCD	Charge-Coupled Device
CMA	Clemmow-Mullaly-Allis
DCT	Discrete Cosine Transform
FFT	Fast Fourier Transform
MHD	Magneto-Hydro-Dynamics
E-beam	Electron beam
eV	Electronvolt

Chapter 1: Introduction

1.1 Plasma: The fourth state of matter

Plasma is a hot ionized gas which is formed of approximately the same number of positively and negatively charged particles, i.e. ions and electrons. It is also known as the fourth state of matter and ~99% of the observable universe consists of plasma. Macroscopically, the plasma medium is described by its temperature and density. Microscopically, plasma is described statistically using distribution functions for calculating the positions and the velocities of particles. The plasma charged particles emit radiation due to their mutual collisions.

The use of "plasma", as a term for an ionized gas, begun in 1927 by Irving Langmuir (1881-1957), an American citizen whose achievements ranged from the surfaces chemistry to the cloud seeding for rain promoting. In 1932, he won the Nobel Prize for chemistry (1), (2). As his co-worker Harold M. Mott-Smith recollected later (3), “[Langmuir] pointed out that the equilibrium part of the discharge acted as a kind of sub-stratum carrying particles of special kinds, like high-velocity electrons from thermionic filaments, molecules and ions of gas impurities”. David A. Frank-Kamenezki identified plasma as the fourth state of matter (4), (5). This view is referred to the four elements of pre-Socratic Greek philosophy: Earth (solid), Water (liquid), Air (gaseous) and Fire. Moreover, the initial idea for a fourth state of matter goes back to Michael Faraday (1791–1867), who, in 1809, speculated about a radiant state of matter. He associated it with the luminous phenomena produced by electric currents that flow in gases. From a phenomenological point of view, the identification of plasma as a new state of matter can be justified because (6) the splitting of neutral atoms into electrons and ions at high temperatures, is associated with a new energy barrier, the ionization energy. Today it is known that plasma is not only the hot, disordered state of matter described above. On the contrary, we have learned over the past 20 years that plasma systems can achieve gaseous, liquid or even solid phases.

1.2 Objectives and Scope of the research

This research is focused on the study of the X-pinch device as a point source of ultra-short X-ray pulses. The research points are related to the study of the plasma jets dynamics (expansion speed), the X-ray emission bursts (pulse width, energy) and the time evolution of the cross-point. Furthermore, measurements were carried out, in order to find the radial density distribution of the plasma and the phase shift of the laser beam at the cross-point.

1.3 Basic plasma parameters

Plasma is characterized by its density, which is tightly connected to its temperature and is given by the following equation:

$$n(\Phi) = n_0 \exp(\frac{e\Phi}{k_B T}) \tag{1.1}$$

where Φ is the electrostatic potential, n_0 is the initial density, e is the electronic charge, k_B is the Boltzmann constant and T is the electron temperature of the plasma. In hot plasmas, $\ll k_B T$, equation (1.1) can be written in a linear form as:

$$n(\Phi) \sim \mathrm{n}\left(1 + \frac{e\Phi}{k_B T}\right) \tag{1.2}$$

We can consider the potential around a point charge at the origin of the coordinate system. Poisson equation is used to find the potential $\Delta\Phi$ assuming spherical symmetry:

$$\Delta\Phi = \frac{1}{\mathrm{r}^2}\frac{\mathrm{d}}{\mathrm{dr}}\left(\mathrm{r}^2\frac{\mathrm{d}\Phi}{dr}\right) = -\frac{\rho}{\varepsilon_0} = \frac{q\delta(r)}{\varepsilon_0} + \mathrm{e}\frac{\mathrm{n_e} - \mathrm{n_i}}{\varepsilon_0} \tag{1.3}$$

where ρ is the total volume charge density, ε_0 is the vacuum permittivity, r is the radius of the volume, δ is the delta function and $\mathrm{n_e}$, $\mathrm{n_i}$ are the electronic and the ionic density respectively.

In case of a point charge in vacuum, the right part of equation (1.3) reduces to a δ–function at $r = 0$, so that for $r \neq 0$ we have $\Delta\Phi = 0$. In this case, we obtain the Coulomb potential which decays radially with $1/r$. In a plasma the second term, the density distribution as a function of the potential energy Φ, is given by the equation (1.2):

$$\mathrm{n_e} - \mathrm{n_i} \approx \mathrm{n_{e,0}}\left(1 + \frac{e\Phi}{k_B T} - \left(1 - \frac{e\Phi}{k_B T}\right)\right) = 2\mathrm{n_{e,0}}\frac{e\Phi}{k_B T} \qquad (1.4)$$

Here, we assumed the quasi neutrality condition, i.e. $\mathrm{n_{e,0}} = \mathrm{n_{i,0}}$ for long distances from the point charge. Under these assumptions the solution of Poisson equation for $r \neq 0$ becomes

$$\Phi(\mathrm{r}) = \frac{\mathrm{q}}{4\pi\varepsilon_0 r}\mathrm{e}^{-\frac{\sqrt{2}\mathrm{r}}{\lambda_D}} \qquad (1.5)$$

where the Debye length λ_D is introduced:

$$\lambda_D = \sqrt{\frac{\varepsilon_0 k_B T}{\mathrm{n_{e,0}}\,\mathrm{e}}} = 7.43x10^2 T^{1/2} n^{-1/2} [cm] \qquad (1.6)$$

For $r \ll \lambda_D$, the exponential term is considered to be approximately equal to ~ 1 and we have the usual Coulomb potential. On the contrary, for $r \gg \lambda_D$, the potential vanishes exponentially, i.e. faster than $1/r$. The Debye length is one of the most characteristic parameters of a plasma. It represents the typical distance over which electrostatic fields are screened.

The index of refraction of plasma is strongly connected with its MHD conditions. It is also related with the plasma frequency as well as with the frequency and the polarization of the incident radiation. Phenomena of propagation, reflection and absorption of radiation, occur after the incidence of an electromagnetic wave. The electromagnetic and electrostatic waves, that are encountered in plasma, are classified according to their polarization and the relative angle to the magnetic field of the plasma (B_0) as presented in Table 1.1.

EM character	Oscillating Species	Conditions	Dispersion Relation	Name
Electrostatic	Electrons	$\vec{B}_0 = 0 \ or \ \vec{k} \parallel \vec{B}_0$	$\omega^2 = \omega_p^2 + 3k^2u_{th}^2$	plasma oscillation (or Langmuir wave)
		$\vec{k} \perp \vec{B}_0$	$\omega^2 = \omega_p^2 + \omega_c^2 = \omega_h^2$	Upper hybrid oscillation
	Ions	$\vec{B}_0 = 0 \ or \ \vec{k} \parallel \vec{B}_0$	$\omega^2 = k^2u_s^2 = k^2\frac{\gamma_e KT_e + \gamma_i KT_i}{M}$	ion acoustic wave
		$\vec{k} \perp \vec{B}_0$ (nearly)	$\omega^2 = \Omega_c^2 + k^2u_s^2$	electrostatic ion cyclotron wave
		$\vec{k} \perp \vec{B}_0$ (exactly)	$\omega^2 = [(\Omega_c\omega_c)^{-1} + \omega_i^{-2}]^{-1}$	lower hybrid oscillation
Electromagnetic	Electrons	$\vec{B}_0 = 0$	$\omega^2 = \omega_p^2 + k^2c^2$	light wave
		$\vec{k} \perp \vec{B}_0, \vec{E}_1 \vert\vert \vec{B}_0$	$\frac{c^2k^2}{\omega^2} = 1 - \frac{\omega_p^2}{\omega^2}$	O wave
		$\vec{k} \perp \vec{B}_0, \vec{E}_1 \perp \vec{B}_0$	$\frac{c^2k^2}{\omega^2} = 1 - \frac{\omega_p^2}{\omega^2}\frac{\omega^2 - \omega_p^2}{\omega^2 - \omega_h^2}$	X wave
		$\vec{k} \vert\vert \vec{B}_0$ (right circ. pol.)	$\frac{c^2k^2}{\omega^2} = 1 - \frac{\omega_p^2/\omega^2}{1 - (\omega_c/\omega)}$	R wave (whistler mode)
		$\vec{k} \vert\vert \vec{B}_0$ (left circ. pol.)	$\frac{c^2k^2}{\omega^2} = 1 - \frac{\omega_p^2/\omega^2}{1 + (\omega_c/\omega)}$	L wave
	Ions	$\vec{B}_0 = 0$		none
		$\vec{k} \vert\vert \vec{B}_0$	$\omega^2 = k^2u_A^2$	Alfvén wave
		$\vec{k} \perp \vec{B}_0$	$\frac{\omega^2}{k^2} = c^2\frac{u_s^2 + u_A^2}{c^2 + u_A^2}$	magnetosonic wave

Table 1.1: Summary of elementary plasma waves, ω - wave frequency, k - wave number, c - speed of light, ω_p - plasma frequency, ω_i - ion plasma frequency, ω_c - electron gyrofrequency, Ω_c - proton gyrofrequency, ω_h - upper hybrid frequency, u_s - plasma "sound" speed, u_A - plasma Alfvén speed (7), (8).

The electron gyrofrequency is defined by ω_c which is the angular frequency of the circular motion of an electron in the plane perpendicular to the magnetic field and is expressed by:

$$\omega_c \frac{eB_0}{m_e} \tag{1.7}$$

where B_0 is the magnetic field and m_e is the electron mass.

The electron plasma frequency with which electrons oscillate, is given by:

$$\omega_p = (\frac{n_e e^2}{\varepsilon_0 m_e})^{1/2} \tag{1.8}$$

The frequency of long wavelength oscillations is a "hybrid", or mix, of the electron plasma ω_{pe} and electron cyclotron ω_{ce} frequencies,

$$\omega_h^2 = \omega_{pe}^2 + \omega_{ce}^2 \tag{1.9}$$

The waves speed that results from the mass of the ions m_i and the restoring force of the magnetic field B is called Alfvén velocity:

$$u_A = \frac{B}{\sqrt{4\pi n_i m_i}} \tag{1.10}$$

The aforementioned propagation modes of the waves, in a magnetized cold plasma ($T_e = T_i \; = 0$), and also the propagation regions, separated in areas defined by the cutoff frequency and resonance, are described by the following diagram.

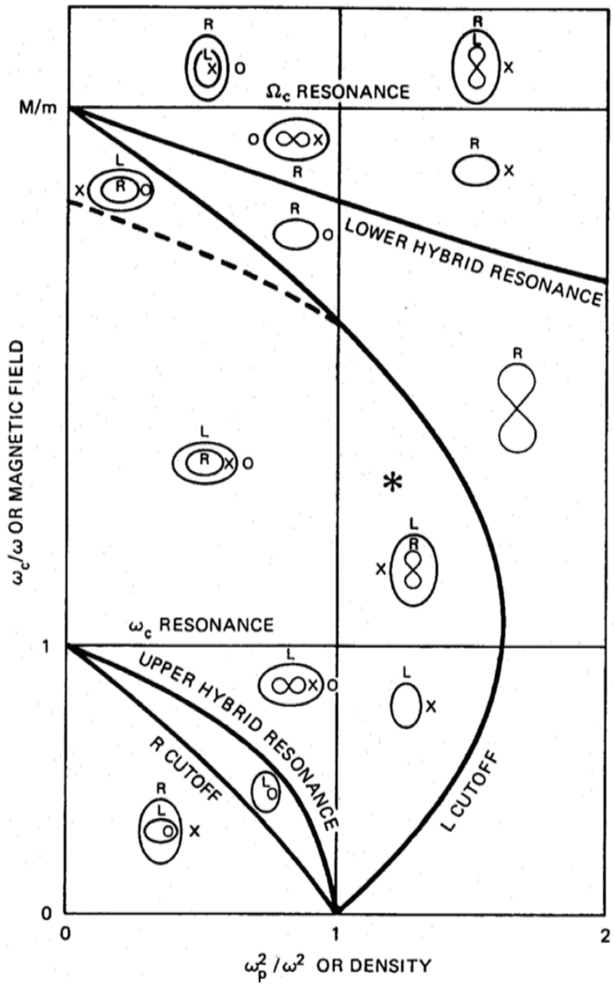

Figure 1.1: Clemmow-Mullaly-Allis (CMA) diagram to study the various propagation ways in "cold" plasma (9).

1.4 Debye Shielding

Plasmas do not carry strong electric fields as they reorganize in order to be shielded from them. Plasma oscillations are stimulated to maintain its macroscopic neutrality. If plasma is subjected to an external electric field, its free charges redistribute so that the plasma is shielded. Suppose an immerse test particle $+Q$ within a plasma with $n_i = n_e = n$. At $t = 0$, the electric potential has the form:

$$\Phi(r) = \frac{1}{4\pi\varepsilon_0}\frac{Q}{r} \tag{1.11}$$

As time progresses, electrons are attracted, while ions are repelled. As $m_i \gg m_e$ the motion of ions is neglected. At $t \gg 0$ and $n_e > n$ a new potential is set up, with charge density: $\rho = e(n_e - n_i)$. The new potential is evaluated using Poisson's equation (1.3). In presence of the potential, the electron number density is:

$$n_e(r) = n_e{}^{-e\Phi(r)/k_B T_e} \tag{1.12}$$

Substituting equation (1.12) into Poisson's equation in spherical coordinates it holds:

$$\frac{1}{r^2}\frac{d}{dr}\left(r^2\frac{d\Phi}{dr}\right) = -\frac{en}{\varepsilon_0}\left[e^{-\frac{e\Phi}{k_B T_e}} - 1\right] \tag{1.13}$$

For $|e\Phi| \ll k_B T_e$ Taylor expansion is used:

$$e^x \approx 1 + x \Rightarrow \frac{1}{r^2}\frac{d}{dr}\left(r^2\frac{d\Phi}{dr}\right) \approx \left[\frac{ne^2}{\varepsilon_0 k_B T_e}\right]\Phi(r) = \frac{1}{\lambda_D^2}\Phi(r) \tag{1.14}$$

where λ_D is the Debye shielding length and it's numerical expression is:

$$\lambda_D \cong 69\sqrt{T_e/n} \tag{1.15}$$

where T_e is in K and n is in m^{-3}.

The typical number of particles in a Debye sphere is given by the plasma parameteρ:

$$N_D = \frac{4\pi n\lambda_D^3}{3} \tag{1.16}$$

The characteristic collective plasma behavior is only observed for time scales longer than the plasma period and for length scales larger than the Debye length. The statistical character of this behavior is controlled by the λ_D ,N_D and ω_p, which are the three fundamental plasma parameters.

1.5 Plasma Criteria

A plasma is described as an electrically neutral medium of positive and negative particles. A more rigorous definition requires three criteria to be satisfied:

- The first criterion concerns particle collisions. If ω_p is the frequency of a typical plasma oscillation and τ is the mean time between collisions with neutral atoms, then $\omega_p\tau > 1$ is required for the gas to behave like a plasma instead of a neutral gas.
- Gas is considered as plasma if its length scale is larger than Debye length. This is the second criterion and $\lambda_D \ll L$.

- Debye Length is a spatial scale over which charge neutrality is violated by spontaneous fluctuations. Debye number is defined at the (1.16) equation. In addition to $\lambda_D \ll L$, “collective behavior” requires:
- $N_D \ggg 1$ and this is the third criterion.

1.6 Interferometry

The interferometry method is based on the principle of the electromagnetic waves superposition. An interferometer is any device in which two or more waves are allowed to interfere by coherent addition of the electric fields. The observed intensity is modulated according to whether the fields interfere constructively or destructively, that means the waves are in phase or out of phase. Measurements of the refractive index of any medium are most often made by some form of interferometry.

Consider $E_1 expi\omega t$ and $E_2 expi(\omega t + \Phi)$ added together to a simple two-beam interferometer, with some phase difference Φ between them. The total field is given by:

$$E_t = (E_1 + E_2 expi\Phi) expi\omega t \tag{1.17}$$

The detected power by a square-law detector is proportional to $|E_t^2|$ and may readily be shown to be:

$$|E_t|^2 = [E_1^2 + E_2^2][1 + \frac{2E_1E_2}{E_1^2 + E_2^2} cos\Phi] \tag{1.18}$$

A constant component plus a varying component like $cos\Phi$ compose the output intensity.

There are several types of interferometers that are used for different purposes. The more common configurations are:

- The Michelson interferometer as illustrated in figure (1.2), is a usual optical set-up for interferometry that was invented by Albert Abraham Michelson. A light source is split into two arms by a beamsplitter (BS). Each of the beams is reflected back toward the beamsplitter which then their amplitudes combines interferometrically. The produced interference pattern, which is not directed back to the source, is usually directed to a Charge-Coupled Device (CCD) camera or some type of photoelectric detector. The two light optical paths can have different lengths or embody optical elements or materials which are under test, for different applications of the interferometer.

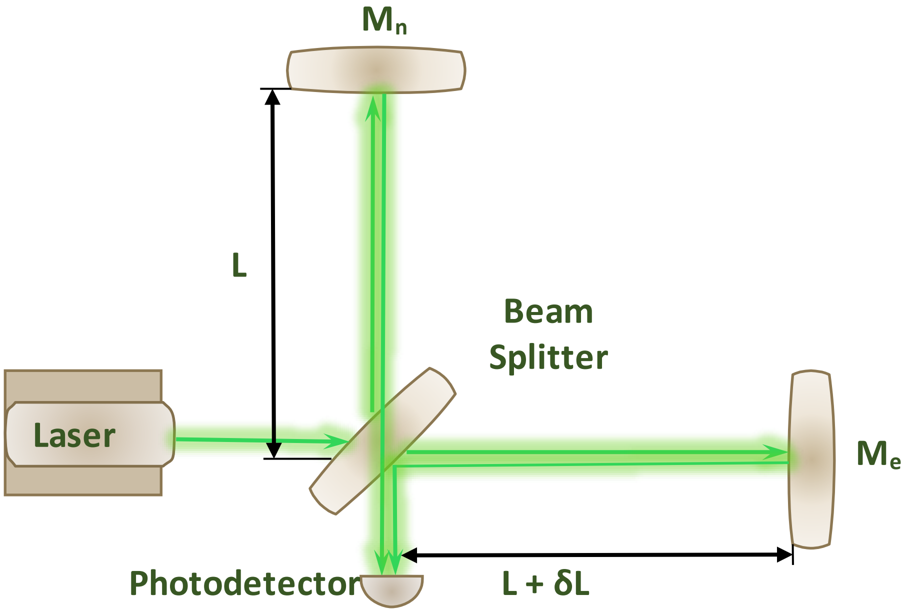

Figure 1.2: Scheme of a Michelson interferometer.

- The Mach–Zehnder interferometer is an optical set up used to specify the relative phase shift changes between two collimated beams, obtained by splitting light from a single source. A collimated beam is split by a beam-splitter. The two resulting beams (the "sample" and the "reference") are reflected by a mirror, then the two beams pass a second beam-splitter and enter the detector (CCD camera).

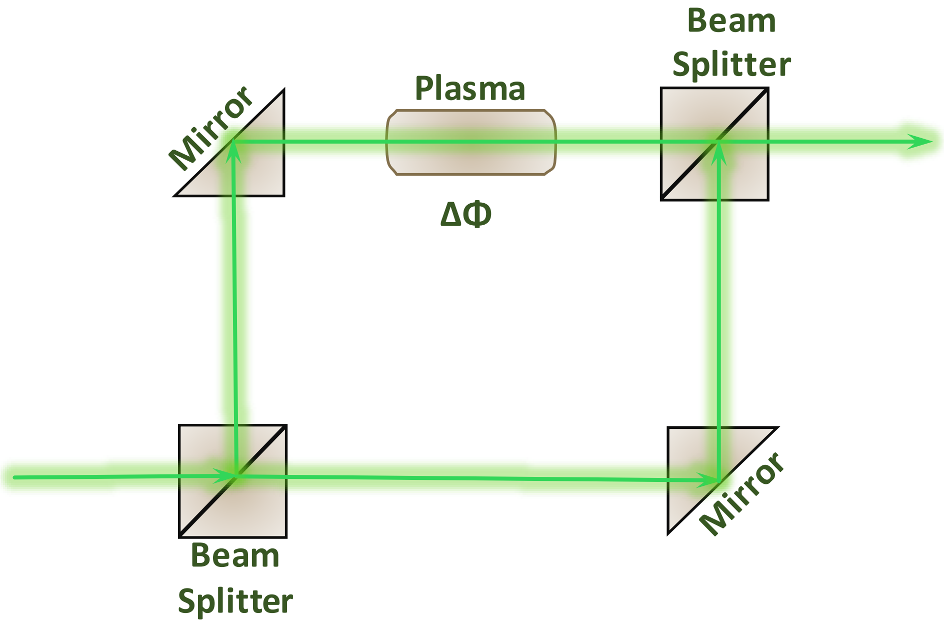

Figure 1.3: Scheme of a Mach-Zehnder interferometer.

- The Fabry–Pérot interferometer (FPI) or etalon is designed in 1897 by C. Fabry and A. Perot and is an evolution of the Michelson interferometer. The difference is that the Fabry-Perot based on the phenomenon of multiple beam interference. It is typically made of a transparent plate with two reflecting surfaces, or two parallel highly reflecting mirrors. It's transmission spectrum as a function of wavelength exhibits large transmission peaks matching to resonances of the etalon. Since it has multiple beams, the output is not a simple cosine as in two-beam interferometers. This makes phase shift interpretation more difficult, so it is often less used for plasma refractive-index measurements.

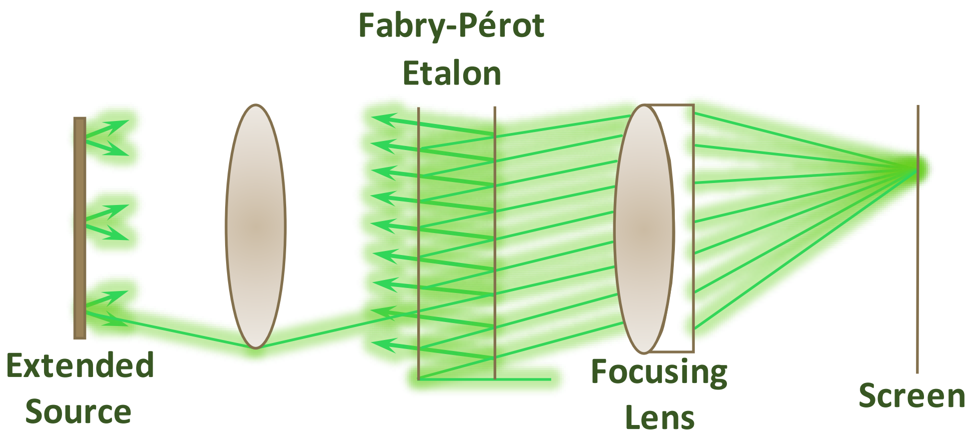

Figure 1.4: Scheme of a Fabry–Pérot interferometer.

In order to measure the refractive index of plasma in one arm of a two-beam interferometer, such as the Mach-Zehnder, the total phase lag in the plasma arm will be:

$$\Phi = \int k\, dl = \int N \frac{\omega}{c} dl \tag{1.19}$$

A significant proportion of the length of this arm along which integration is considered, will be outside the plasma. Furthermore, the reference arm has a length and a corresponding phase lag that may not be known with great precision. These effects are all removed by comparing the phase difference between the two arms, with plasma present to that without plasma. The difference in these phases is then simply introduced into the plasma arm:

$$\Delta\Phi = \int \left(k_{plasma} - k_0\right) dl = \int (N-1) \frac{\omega}{c} dl \tag{1.20}$$

where k_0 is the free-space wavenumber, k_{plasma} is the plasma wavenumber and N is the refractive index.

By assuming that in the absence of plasma $k_0 = \omega/c$, the wave propagates effectively in vacuum. The integral is now considered to be limited to that part of the path that lies in the plasma.

The interferometer phase shift measurement $\Delta\Phi$ provides us with a measure of the mean refractive index along the line of the interferometer beam through the plasma.

The plasma refractive index is given by the following equation:

$$N^2 = 1 - X = 1 - \frac{\omega_p^2}{\omega^2} = 1 - n_e/n_c \tag{1.21}$$

where n_c is the cutoff density, given by:

$$n_c \equiv \omega^2\, m\varepsilon_0/e^2. \tag{1.22}$$

For $n_e < n_c$ the phase shift in relation to electron density is given by:

$$\Delta\Phi = \frac{\omega}{c}\int\left[\left(1 - \frac{n_e}{n_c}\right)^{\frac{1}{2}} - 1\right]dl \tag{1.23}$$

while for very small plasma density it holds $n_e \ll n_c$ and an approximate expansion is:

$$N \approx 1 - \frac{1}{2}(n_e/n_c) \tag{1.24}$$

and the phase shift simplifies to:

$$\Delta\Phi = \frac{-\omega}{2cn_c}\int n_e dl \tag{1.25}$$

For density above the cutoff value $n_e > n_c$, N becomes imaginary. In this case, the wave is no longer propagating but reducing exponentially with distance (6).

1.7 Shadowgraphy

Shadowgraphy is the simplest optical imaging method based on the divergence of the light, due to refraction as it passes through an object. The shadow that appears on a surface perpendicular positioned on the optical axis and behind the object is the projection of the object on the surface. With this diagnostic method we can obtain information about the pinch dynamics and the electron density through the indirect measurement of the refractive index (10). The shadowgraphy method is more precise over other methods of phase reconstitution. The following image illustrates the shadowgraphy method optical setup.

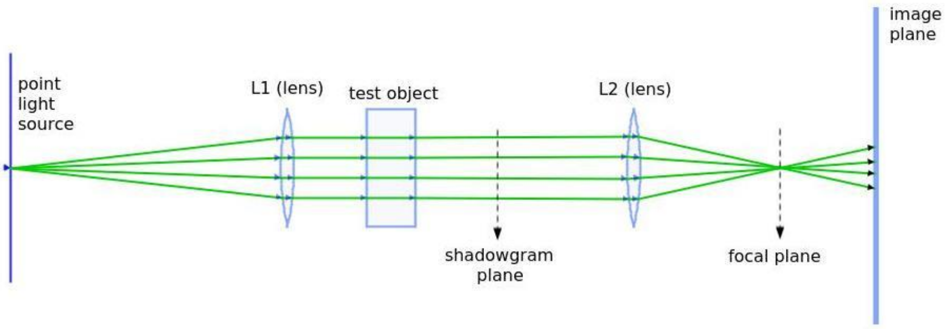

Figure 1.5: Shadowgraphy optical system.

The lens L2 is used in order to image the shadowgram's idol on the image plane. The idol is formed on the imaginary shadowgram plane at a specific length from the test object. The benefit of using a focal lens (L2) is that we can adjust the resolution of the image by choosing the appropriate distance. The disadvantage is that the overall field is limited by the diameter of the lens.

Areas of different brightness are presented on the image plane because of the diverted rays, at angles proportional to the gradient of the refractive index on the vertical plane. These changes are proportional to the light intensity and also to the second spatial derivative of the refractive index in the vertical plane (11), (12).

$$\left(\frac{\partial^2}{\partial x^2}+\frac{\partial^2}{\partial y^2}\right)\int_0^D \eta_{(x,y,z)}\,dz=-\frac{1}{L}\frac{I_{(x,y)}-I_o}{I_o} \tag{1.26}$$

The Poisson's equation includes as a source, the relative value of the disturbed intensity ($I_{(x,y)}$), normalized to the reference intensity (I_o). The solution of the equation can provide us information about the optical paths $(x, y, 0 \leq z \leq D)$ through the plasma. Furthemore, by using the Abel inversion transformation we can reconstitute the refractive index $\eta_{(x,y,z)}$ as mentioned before (6).

1.8 Basics of the Z-pinch physics

The Z-pinch is a pulsed power generator that uses the self-generated magnetic field of the current-carrying straight wire to compress the produced plasma (13). The experimental production of Z-pinches dates as far back as 1790 when Martinus van Marum, a Dutch scientist discharged 1 kJ of energy stored in Leyden jars through a wire, causing its subsequent vaporization (14). In 1905, the electromagnetic pinch effect, was first explained, when a lightning struck a copper tube that served as a lightning rod in New South Whales at a kerosene refinery, and crushed portions of the tube (15). Two years later, the 'pinch' term was used by Edwin Northrup, describing the effect he observed when high currents interacted with a trough of mercury (16). He noted that at certain points, the fluid would form V-shaped depressions in its otherwise uniform distribution in the trough. With an adequate increase in current, he observed that the depression would steepen, reaching the bottom of the trough, disrupting the circuit. W. H. Bennett in 1934 presented a relationship among line density, temperature and current for streams of charged particles (17). The relation he developed can extend to the field of the magnetic confinement of plasmas although his work did not directly refer to it.

1.9 MHD Plasma instabilities

MHD instabilities play a critical role in the dynamics of exploding wire experiments (18-22). They dictate the plasma behavior in most plasma geometries and plasma regimes (23). Any disturbance that may occur in a plasma parameter such as temperature, density, magnetic or electric field, or even in the current, result in MHD instabilities (23). The driving current is not only increasing the temperature of the plasma through electromagnetic forces, but also produces a magnetic field around the plasma column which thermally insulates the hot plasma from the wall and exerts an inward radial force that confines the plasma into a tight column. Such a tight plasma structure can transfer efficiently the electrical energy into intense radiation, but at the same time is unstable due to certain plasma instabilities. These instabilities impose several limitations on the amount of current and pressure that can be confined by the magnetic field (24). The pressure due to the magnetic field around the plasma column is given by:

$$P_{mag} = \frac{B^2}{2\mu_0} = \frac{\mu_0 I_0^2}{8\pi^2 r^2} \tag{1.27}$$

where I_0 is the current flow through the wires and $\mu_0 = 4\pi \times 10^{-7} T \cdot m/A$ is the permeability of vacuum.

The current flow results in the creation of a counterforce against the magnetic pressure, which is expressed as a thermal or kinetic force of the plasma ∇P_{kin}. It holds that

$$P_{kin} = n_e k_B T_e + n_i k_B T_i \tag{1.28}$$

which is the equation of state for ideal gas where k_B is the Boltzmann constant, n_e and n_i are the electron and ion density, T_e and T_i are the electron and ion temperature.

1.9.1 Sausage m=0 and kink m=1 instability

The sausage and kink instabilities are also named as $m = 0$ and $m = 1$ instabilities ($e^{im\theta}$) which is their poloidal mode number.

The sausage instability occurs in regions where the plasma column narrows. In this case, the magnetic field increases locally due to the local increase of the current flow. Therefore, in this region, the magnetic pressure pushes the plasma strongly inwards and finally the plasma column collapse.

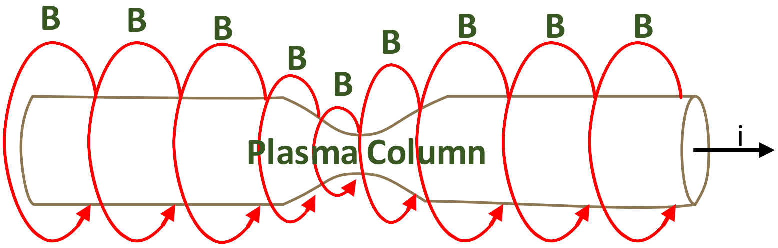

Figure 1.6: Illustration of sausage instability (m=0).

The reduction of this instability requires the existence of an axial magnetic field B_z. The compression of the cross-section increases locally the magnetic field whose increased pressure resists further reduction of the cross-section of the plasma column.

The kink instability occurs when the magnetic field increases on the one side of the plasma column and decreases on the opposite (on specific region) which this leads the region to bend. This type of instability can develop in a thin plasma column carrying a strong axial current.

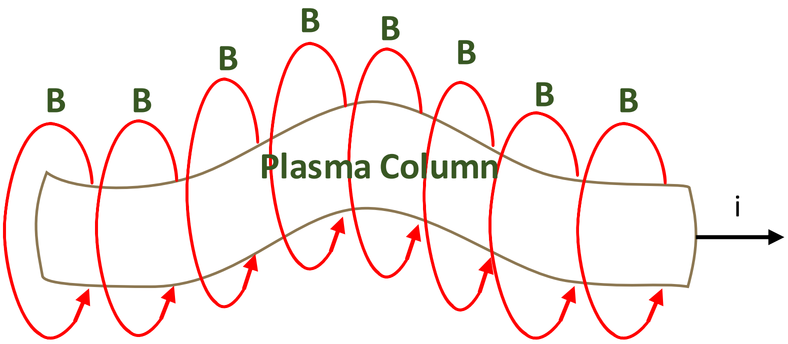

Figure 1.7: Illustration of kink instability (m=1).

Also, in this case the only way to reduce this instability is by introducing an axial magnetic field B_z. The strain of the curved B_z acts toward the center of the bending and neutralizes the effect of increasing the magnetic field due to the increase of the B_φ inside the bending. It turns out that when $B_z \approx B_\varphi$ then the column is stable.

1.9.2 Rayleigh-Taylor instability

The Rayleigh–Taylor instability happens in inhomogeneous plasma. This type of instability appears among two fluids with different densities when the lighter fluid pushes the heavier fluid.

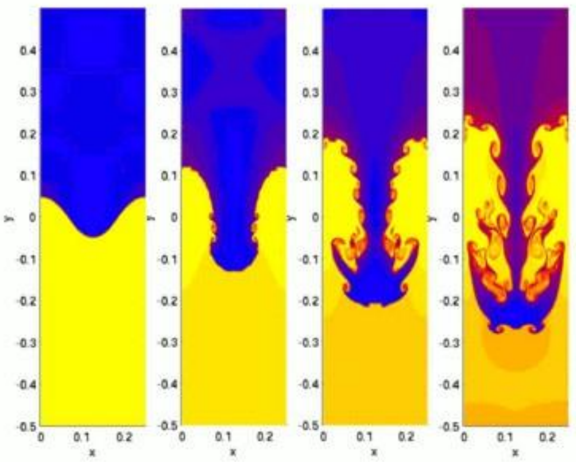

Figure 1.8: Hydrodynamics simulation of a single "finger" of the Rayleigh–Taylor instability (25).

The magnetic field acts as the light fluid pushes the plasma and the growth rate of the perturbation is expressed by the following equation:

$$\gamma = \sqrt{gk} \tag{1.29}$$

where g is the acceleration due to the gravity and k is the wave number of instability (24).

1.10 X-ray production

One of the processes of X-ray production requires a fast-moving electron beam which is somehow decelerates or stops. When an electron slows down, emits radiation of energy equal to the amount of energy lost by the moving particle, due to the energy conservation principle. This can happen when an electron interacts with the Coulomb potential of a positively charged particle, in which the electron slows down and loses energy. The radiation produced by the process described above is called radiation Bremsstrahlung and has a continuous spectrum.

Another X-ray emission procedure occurs when an electron has the proper amount of energy to extract a bonded electron from the inner core layer of an atom during the interaction. This results in an electron transition from an upper energy layer to the inner energy layer of the atom by emitting X-rays of constant energy, which is specific to each atom depending on the transition that will occur. Thus, is defined the emission and absorbance spectra which is specified for each material.

The K and L emission lines (in keV) for the tungsten, which is the material used as a target in our study, and also for the copper, the aluminum and the titanium that are used as filters of the photodiodes, are presented in the following table. Additionally, the X-ray radiation production procedure is depicted in figure 1.9.

	Ka1	Ka2	Kb1	La1	La2	Lb1	Lb2	Lg1
W	59.31824	57.9817	67.2443	8.3976	8.3352	9.67235	9.9615	11.2859
Cu	8.04778	8.02783	8.90529	0.9297	0.9297	0.9498	-	-
Al	1.48670	1.48627	1.55745	-	-	-	-	-
Ti	4.51084	4.50486	4.93181	0.4522	0.4522	0.4584	-	-

Table 1.2: Spectral emission lines for W, Cu, Al and Ti.

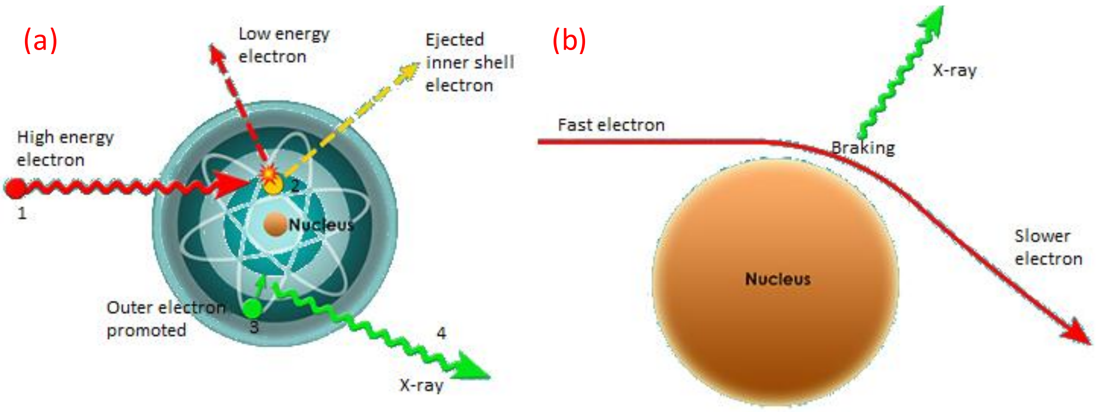

Figure 1.9: (a) Characteristic X-ray generation, (b) Bremsstrahlung/Braking X-ray generation (26).

1.11 X-pinch radiography in comparison with classical radiography

With the classical X-ray tubes which are used for radiography we can achieve very low efficiency, from 0.1 to approximately 20 keV. The achieved pulse duration is approximately 0.1 μs. On the contrary, with the X-pinch devices X-rays with a pulse duration of a few nanoseconds can be produced. This means that with so narrow in time pulses, the distinguishing capacity is increased, and more detailed images can be obtained. The main advantage of the X-pinch devices in relation to X-ray tubes is that they provide very focused X-ray sources with high-intensity. This means that with X-ray tubes we can have high energetic X-ray pulses but not that well focused (27).

1.12 X-pinch plasmas

An X-pinch is formed by two or more fine wires that cross at a single point in the form of an X and is driven by a large current pulse from a pulsed power device. The currents through each of the wires of an n-wire X-pinch combine at the cross-point and the magnetic pressure at that location increases as n^2 relative to a single wire. A localized pinch column is created due to the increased magnetic pressure (28). The column undergoes instabilities that cause an implosion of the plasma into small high temperature and density regions, often referred to as micropinches. From these regions, sub-nanosecond X-ray bursts are emitted. The emission occurs from the center of the X-pinch that acts as a near instantaneous (sub-nanosecond) point source. In the X-pinch plasmas at the stage of the final compression, the surface between the magnetic field and the plasma is very unstable. This happens due to very strong opposite forces: the strong magnetic field and the thermal pressure of the plasma.

The characteristics of the emitted electromagnetic radiation from a X-pinch machine depend on the material and diameter of the wires as well as the electrical characteristics of the generator. Usually the diameter of the metallic wires varies from 10 to 50 μm and the current characteristics vary from 40 kA to 1 MA with a rise time of 40 ns to a few microseconds (24). The main disadvantage is that the repetition rate tends to be very low, and the cost of experiments (especially experiments requiring facility modifications) is very high. A limitation of the X-pinch machine is the needed time to load the wires in the anode-cathode gap by hand and then pump the system down to its operating pressures of 10^{-4} mbar (29).

1.12.1 Low current X-pinch plasmas

X-pinches conducted with a 40 kA peak current and a 10-90% rise time of 30 ns, have successfully produced finely spatially resolved X-ray sources (<10 μm) (30). The 40 kA pulses set the lower limit for the current in X-pinch experiments. Chittenden et al. used a simple model to explain spot formation with such a low current (31). They assumed that during the collapse of a cylindrical micro Z-pinch the radial thermal pressure gradient is balanced by the $\nabla p = J \times B$ force, under which condition, the average electron temperature is given by the Bennett relation

$$8\pi N_i k_B (Z^* T_e + T_i) = \mu_0 I^2 \tag{1.30}$$

where k_B is the Boltzmann's Constant, Z^* is the average ionic charge, I is the total beam current and T_e , T_i are the electron and ion temperatures respectively.

The Ohmic heating due to the current is approximately balanced by the radiation loss rate, which at these densities is predominantly a black body source (32).

2.1 Diagnostics

2.1.1 Current measurement

The Rogowski coil is a simple and effective device for measuring the discharge current in DPP devices (33). It is a current transformer consisting of a multi turn solenoid in a torus form that encircles the discharge current to be measured as shown in Figure 2.1. The discharge current measured by Rogowski coil is directly proportional to the time derivative of the current and the signal must be integrated in order to derive the current. The time derivative of the current can be integrated using an analogue electrical integrator, however it is better to post process the signal and afterwards numerically to achieve better accuracy. This makes a Rogowski coil a more reliable and flexible diagnostic tool.

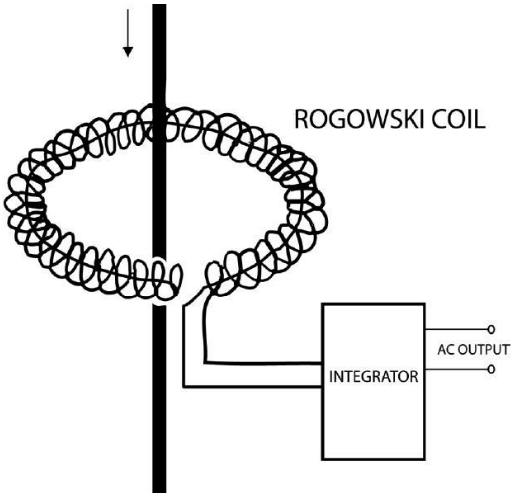

Figure 2.1: Rogowski coil schematic (34).

However, the Rogowski coil has a relatively large inductance that limits its time response to about 13-14 ns, which is inefficient for detection of relatively fast changing current in our X-pinch device. A groove which acts as a single turn Rogowski coil has been designed and used to monitor the discharge current of miniature X-pinch device. The schematic of the Rogowski groove is shown in the following figure:

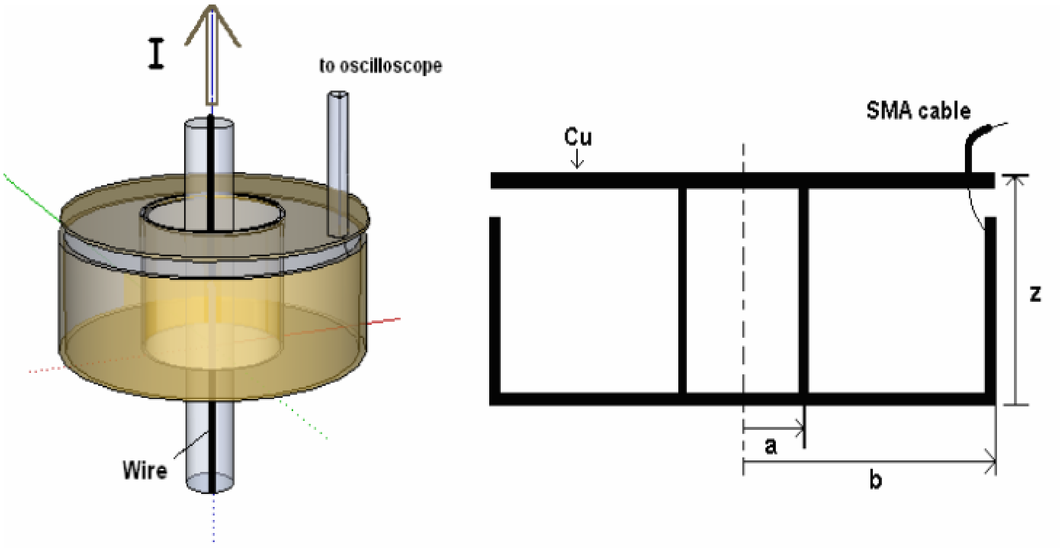

Figure 2.2: Rogowski groove schematic.

The current I flows through the wire and induces a magnetic field B inside the Rogowski Groove:

$$B = \frac{\mu_0 I}{2\pi r} \tag{2.1}$$

where r is the radial distance from the center of the Groove.

By Faraday's Law:

$$V_{groove} = \frac{d\Phi}{dt} = \frac{d}{dt}\int B.ds \tag{2.2}$$

By using 2.1 in 2.2, we have:

$$V_{groove} = \frac{d}{dt}\int_a^b \frac{\mu_0 I}{2\pi r}.zdr = \frac{\mu_0 z}{2\pi}\left(ln\frac{b}{a}\right)\frac{dI}{dt} \tag{2.3}$$

where a is the outer radius of the inner tube, b is the inner radius of the outer tube, z is the depth of the groove, r is the radial distance from the center, Φ is the magnetic flux and μ_o is the permeability of the free space.

For the Rogowski Groove of our X-pinch device it holds that: $a = 5\ mm, b = 15\ mm, z = 8\ mm$ (24).

2.1.2 X-ray measurement

A set of three filtered BPX65-PIN diodes with rise time 12 ns is designed to measure the X-ray fluence in the range of 1 keV to 10 keV. The filters included Al (10 um), Cu (15 um) and Ti (15 um). The detector masked with a Cu filter responds to X-rays in the energy range of 4–9 keV and has the highest transmission response in the energy range that includes the W-L_{a1} (8.3976 keV), W-L_{a2} (8.3352 keV) emission lines. The detector masked with an Al filter allow X-rays above the energy range of 3 keV and the detector masked with a Ti filter allow X-rays above the energy range of 6 keV.

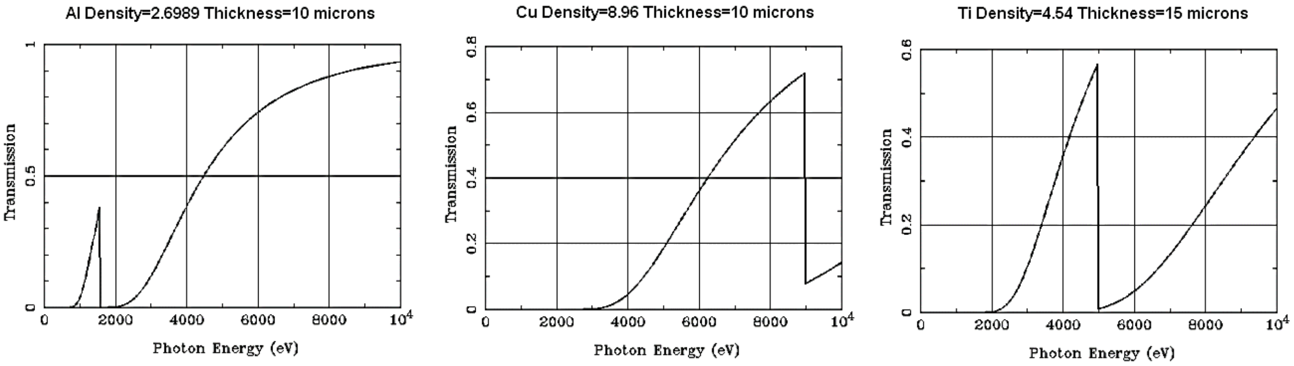

Figure 2.3: Filters Transmission Al (10 um), Cu (10 um), Ti (15 um).

The following table classifies the diagnostics that were used during the X-ray measurements, based on their discretion ability at the tungsten emission spectrum.

	Ka1	Ka2	Kb1	La1	La2	Lb1	Lb2	Lg1
highest	PMT	PMT	PMT	PD Al	PD Al	PD Al	PD Al	PD Al
height				PD Cu	PD Cu	PD Ti	PD Ti	PD Ti
medium				PD Ti	PD Ti			PD Cu
low								PMT

Table 1.3: Discretion ability of the X-ray diagnostics.

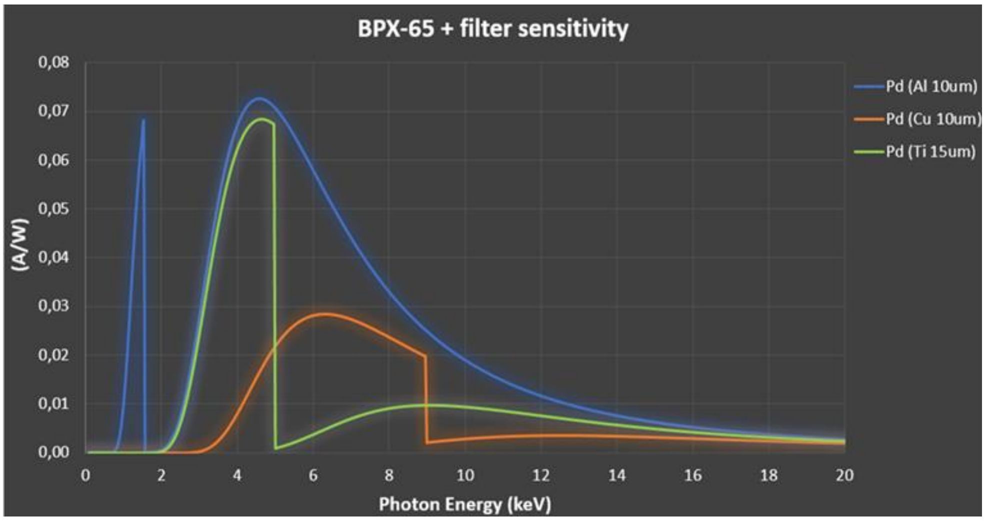

Figure 2.4: Photodiode PIN BPX65 spectral curves with filters plugged.

A fast timing plastic scintillator EJ-228ELJEN TECHNOLOGY and a PMT (photomultiplier) tube assembly H1949-51 HAMAMATSU were used in order to measure the Hard X-ray (HXR) bursts.

The scintillator placed in a light reflector made of aluminum foil. High vacuum grease was used to adapt the front unit of the photomultiplier with the scintillator to avoid reflections. The final unit is placed in a box covered with aluminum foil, in order to be shielded against the electromagnetic noise.

Figure 2.5: (a) photomultiplier and (b) scintillator.

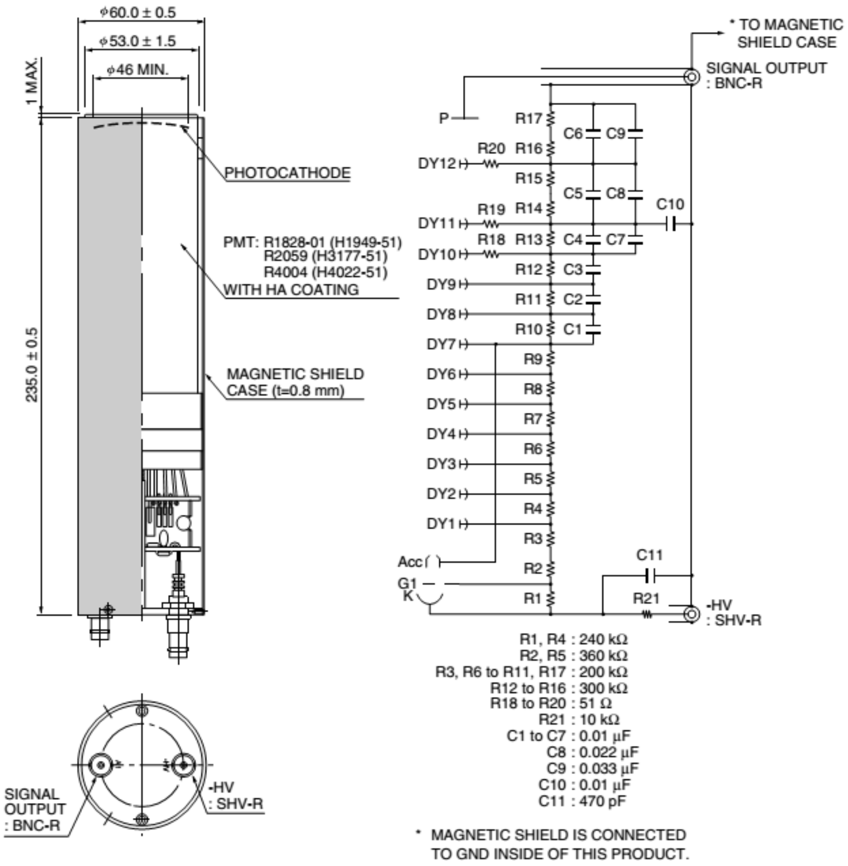

Figure 2.6: Photomultiplier Tube Assembly Dimensional Outline and Diagram (Unit: mm) (35).

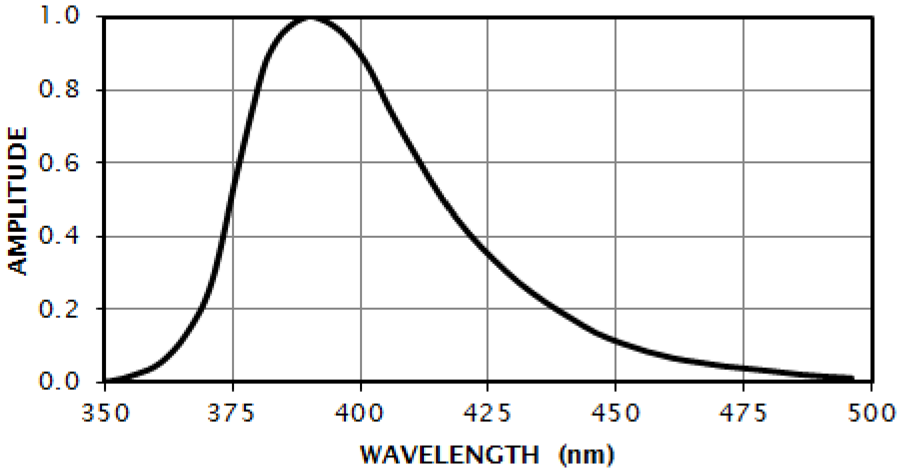

Figure 2.7: ***Scintillator EJ-228 emission spectrum.***

The properties of the photomultiplier and scintillator are presented in the following table (36), (35):

Plastic scintillator EJ-228(Eq. BC-418)		**H1949-51 PMT ASSEMBLY**	
Wavelength of Max. Emission	391 nm	Gain at 2.4kV	1 x 10^7
Rise Time	0.5 ns	Pulse Linearity (5%) typ.	200 mA
Decay Time	1.4 ns	Rise Time	1.3 ns
Pulse Width (FWHM)	1.2 ns	Transit time typ.	28 ns
Scintillation Efficiency	10,200 photons / 1MeV e^{-1}	Wavelength range	300-650 nm

Table 2.1: Photomultiplier and scintillator properties.

2.1.3 Interferometry and shadowgraphy diagnostics

A three frame Mach–Zehnder interferometer was set up and used as a diagnostic tool. The interferometer setup is properly modified to perform also shadowgraphy by cutting-off the reference beam. The optical setup consists of two parts, the laser’s optical table setup (as seen at the following figure) and the interferometer-shadowgraphy, optical table setup.

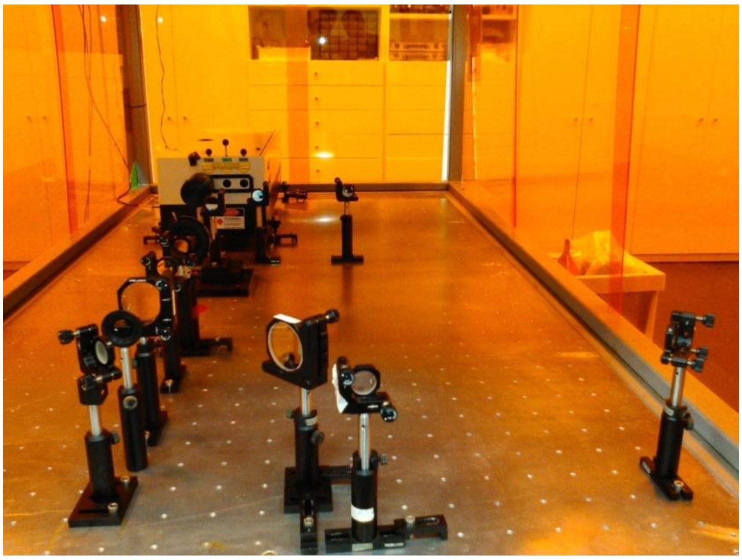

Figure 2.8: Beam expander and collimator setup (setup in front of the beam) and optical delay unit.

The beam expander and collimator unit, was built to provide a wide enough beam with a planar wavefront, in order to cover the entire plasma frame. The following schemes illustrate the optical paths of the beams through the laser's optical table.

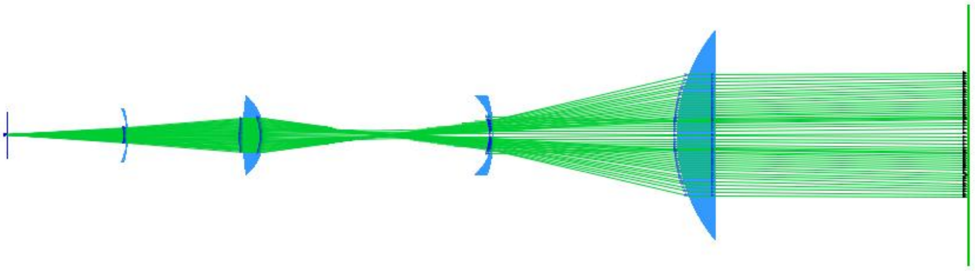

Figure 2.9: Beam expander and collimator unit.

The following optical setup induces the delay between the beams, where each beam propagates in a different optical path until they reach the main optical table. The light needs 3.33 ns to propagate 1 meter in the air. The optical paths have been calculated to create the necessary time delay between the three laser beam paths.

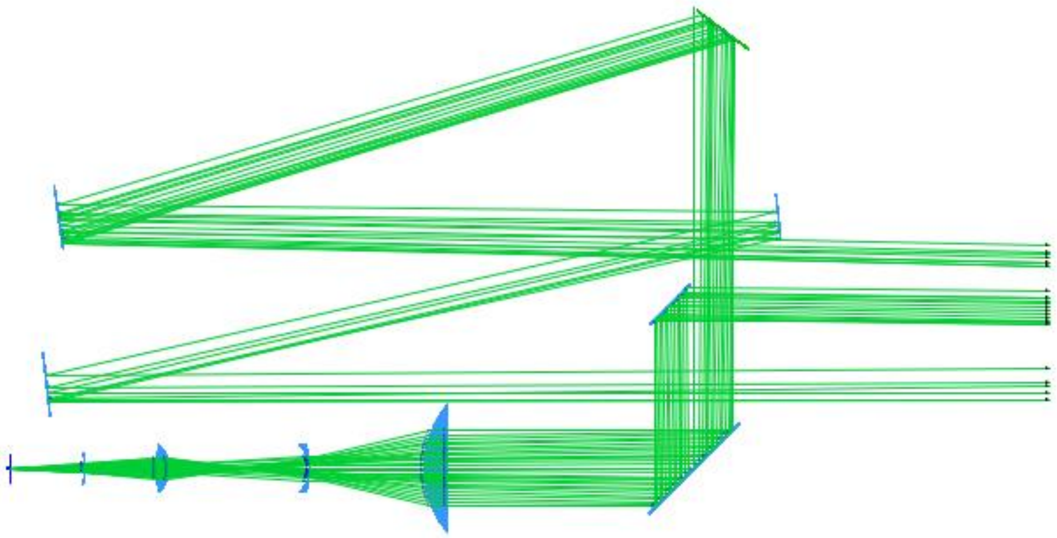

Figure 2.10: Illustration of the optical paths on the laser table.

The following figure illustrates the optical paths of the three time delayed laser beams. The time delay between the first and the second beam is 8 ns, while the delay between the first and the third beam is 15 ns. A part of each beam propagates through the plasma in the vacuum chamber and another part propagates outside the chamber referred as reference beam. Therefore, these two parts of each beam compose their superposition on the CCD cameras. The refractive index of the plasma causes phase shift to the part of the beam which propagates through it. Thus, the final image will have curved fringes in the regions where plasma exists.

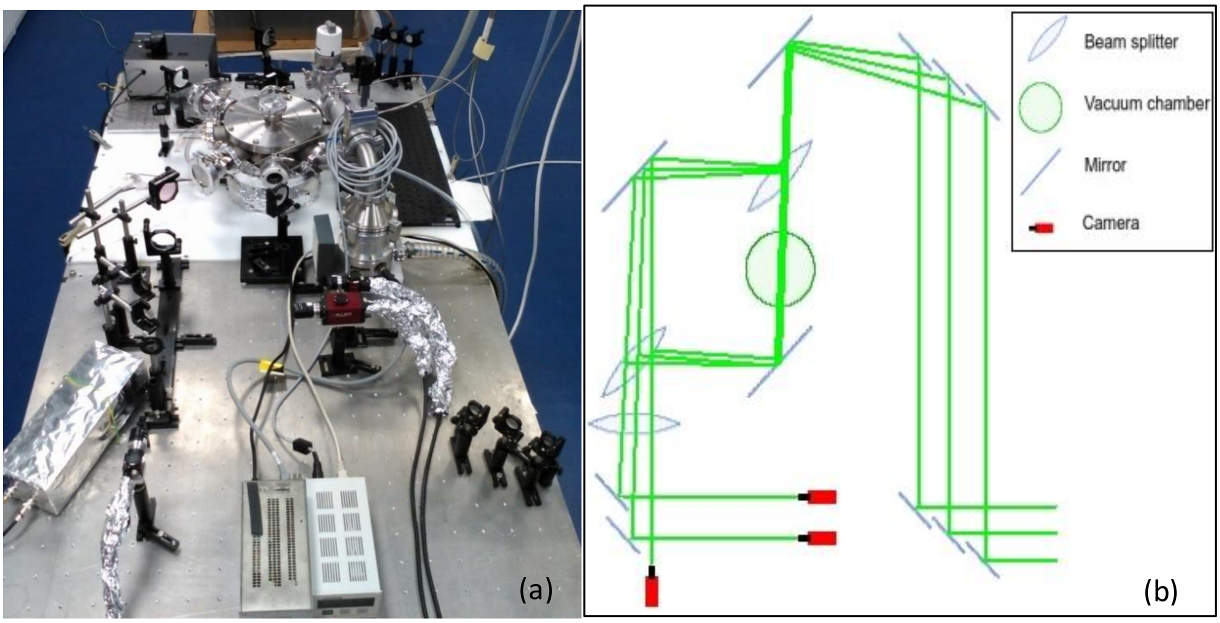

Figure 2.11: (a) Interferometer (b) schematic diagram of the Interferometer.

The laser source used during the experiments is a Q-switched, Nd:YAG EKSPLA SL312 with central wavelength 532 nm and pulse duration 150 ps.

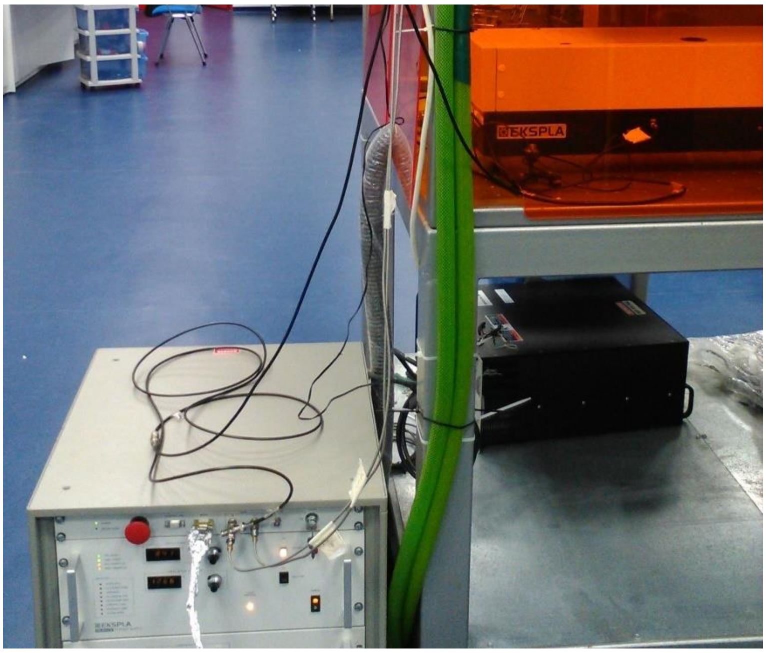

Figure 2.12: Laser source.

The advantage of the selected experimental setup is that in one shot three images in sequence with controlled time difference between them are captured. Therefore, fewer shots are needed to perform in order to have a complete view of the plasma evolution.

2.2 Experimental setup

The X-pinch system is composed of the following parts:

i) Vacuum Chamber

A vacuum chamber is a rigid enclosure from which air and other gases are removed by a vacuum pump and is made of high purity stainless steel. A Rogowski groove is placed on one of the current return posts to measure the current flow and a photodiode placed inside the chamber is used to measure the Soft X-ray (SXR) radiation, i.e. the L emission lines of the tungsten.

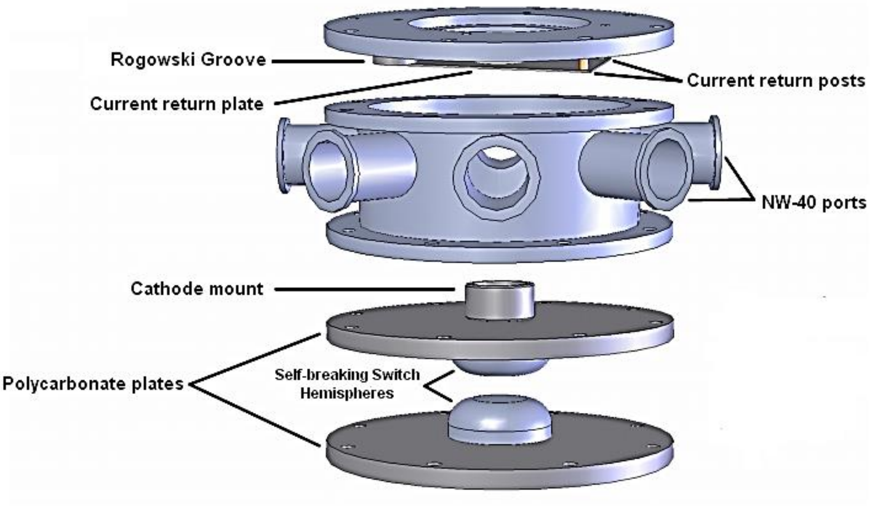

Figure 2.13: The gas switch and vacuum chamber in exploded view (32).

ii) PFL unit

The Pulse forming Line is made of two aluminum cylinders filled with de-ionized water (dielectric) and it acts as a cylindrical capacitor, storing the delivered charge by the Marx bank. A V-Dot detector plugged in the inner surface of the outer cylinder is used to measure the voltage of the PFL.

iii) Marx Bank

The Marx bank is a pulsed power generator containing four capacitors (0.2 μF, 50 kV each). Its purpose is to generate a high-voltage pulse from a low-voltage DC supply. The circuit generates a high-voltage pulse by charging a number of capacitors in parallel, then suddenly connecting them in series. The spark gaps, which are used as switches, have the capacitor's voltage (V_C) across them, but the gaps have a breakdown voltage greater than V_C, so they all behave as open circuits while the capacitors charge.

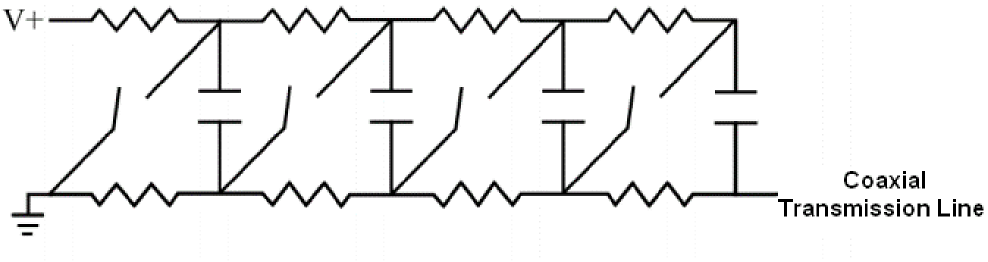

Figure 2.14: Circuit diagram of the Marx Bank with resistors to charge in parallel and switches to discharge in series (32).

iv) Spark gap

A spark gap consists of two electrodes separated by a gap filled by Sulfur hexafluoride SF6 gas, which is an excellent electrical insulator. When the voltage difference between the conductors exceeds the breakdown voltage of the gas, a spark is created in the gap as a result of the ionization of the SF6 gas and reduction of its electrical resistance. Then the current flows until reaching the holding current which means a minimum value. In our case the pressure for the spark gap of the PFL is calculated according to the current to be 1.4 bar. The pressure in the spark gap of the Marx Bank needs to be 1.3 bar.

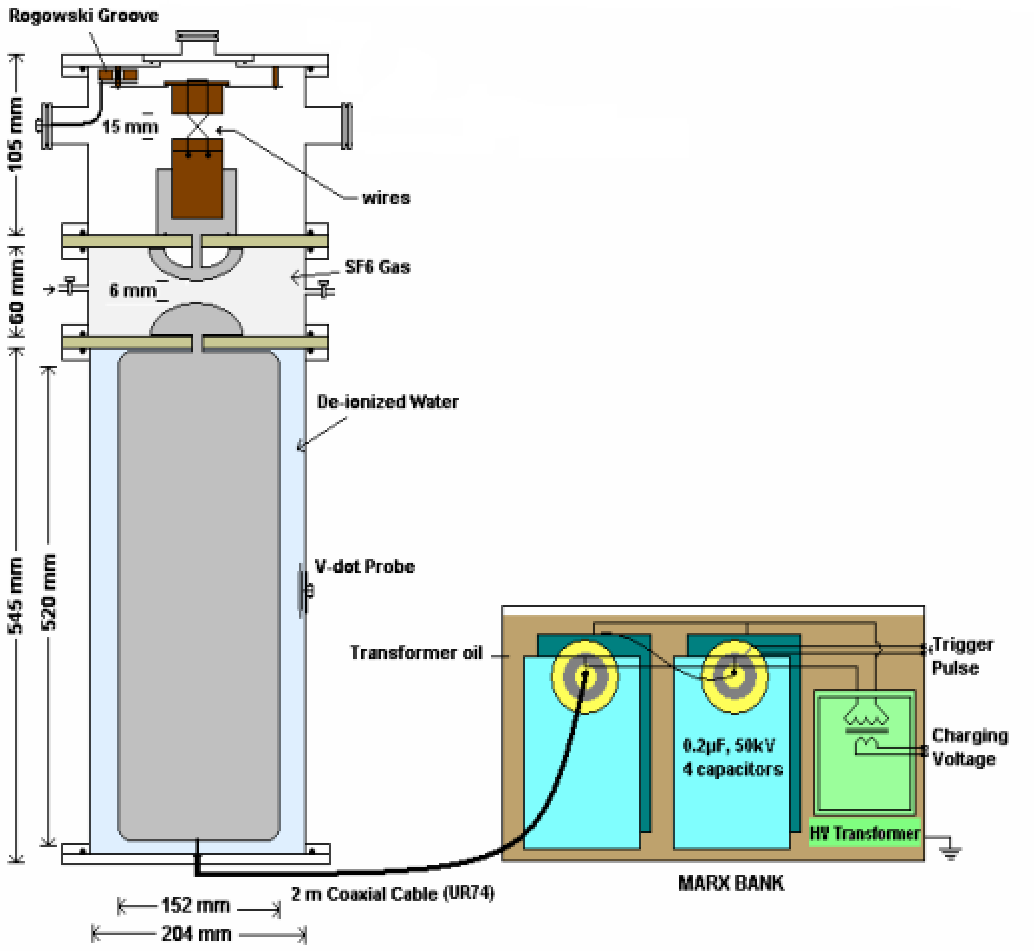

Figure 2.15: Schematic of the X-pinch system (24).

Chapter 3: Results & Discussion

3.1 Data analysis

The software packages that were used to analyze the data, were the SciDAVis for the row data and the IDEA to obtain the phase shift and the density distribution as presented in the following paragraphs (37).

3.1.1 Signals processing

The detected signals propagate at different distances through the wires until they reach the oscilloscope. The time delay induced to each signal is 5.5 ns/m. The length of the cable connecting each diagnostic to the oscilloscope was measured in order to find the exact delay of each signal. The time delay of each signal was used as a parameter to synchronize them.

The following figure shows the interface of SciDAVis during the signals processing. The left graph illustrates with black line the signal from channel 2 (PD laser signal), with red line the channel 4 (PD 10um SXR) and the channel 3 with green line (PMT HXR). The signals on the left graph are adjusted in time depending on the delay of each signal. The right graph illustrates the integrated current.

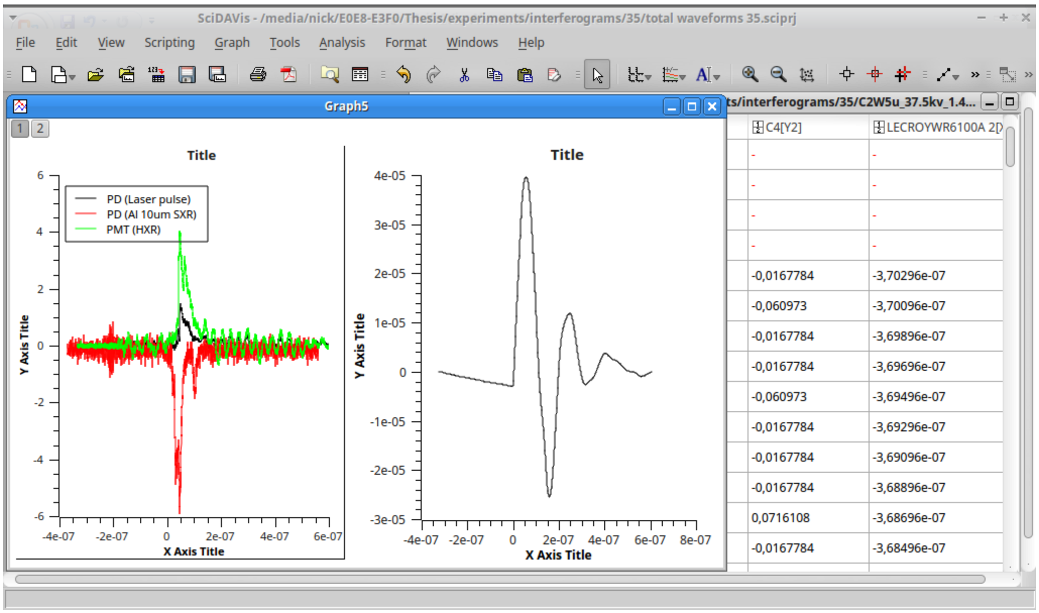
SciDAVis - /media/nick/E0E8-E3F0/Thesis/experiments/interferograms/35/total waveforms 35.sciprj

ts/interferograms/35/C2W5u_37.5kv_1.4...

C4[Y2]	LECROYWR6100A 2[)
-	-
-	-
-	-
-	-
-0,0167784	-3,70296e-07
-0,060973	-3,70096e-07
-0,0167784	-3,69896e-07
-0,0167784	-3,69696e-07
-0,060973	-3,69496e-07
-0,0167784	-3,69296e-07
-0,0167784	-3,69096e-07
-0,0167784	-3,68896e-07
0,0716108	-3,68696e-07
-0,0167784	-3,68496e-07

Figure 3.1: SciDAVis interface left graph (black line laser signal, red line SXR signal, green line HXR signal),right graph (integrated current), background (data).

The next figure illustrates the original signals that are captured from the oscilloscope.

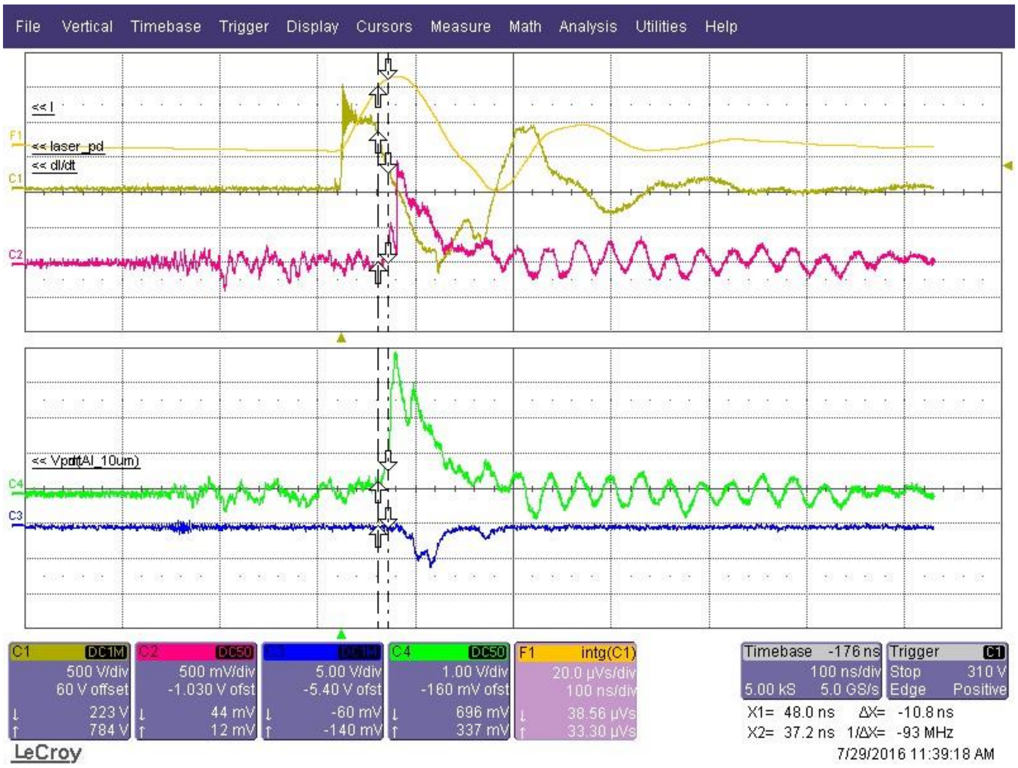

Figure 3.2: C2 red line laser signal, C4 green line SXR signal, C3 blue line HXR signal, F1 orange line integrated current, C1 brown line product of current.

3.1.2 Interferometric analysis

In order to obtain the phase shift and density distribution we used the free license software IDEA which has been developed at the Graz University of Technology (37). The software contains the following main features:

- Phase-Shifting Algorithms
- 2D-Fast Fourier Transformation
- Spatial Phase Shifting and methods for Speckle interferometry with phase shifting in reference state only
- Reconstruction algorithms for digital holograms
- Phase-Unwrapping by Scanning Methods, Branchcut or Fast Cosine Transformation
- Abel-Inversion by f-Interpolation, Fourier Synthesis, or Backus-Gilbert Technique

- Tomographical Reconstruction by Convolution or Algebraic Reconstruction Technique

and also contains additional features:

- Multiple File Manipulation
- Animation
- Interactive Pseudo-Color Viewing
- 2D-Data Field and Image Manipulation
- Spatial Filtering
- Interferogram Simulation

The method used to analyze the interferograms, is the Discrete Cosine Transform (DCT) for the phase unwrapping. The interferometric analysis is as follows:

i) Forward FFT

Fast Fourier Transformation is applied to Image or 2D-Data. The resulting data contain complex amplitudes of all frequencies and are presented by an image, which shows the modulus of the complex amplitudes after mapping data in quad-root mode. The amplitude of zero frequency, which is located in the center of the visualization, was ignored. Coordinates in the Status Bar represent periods of horizontal and vertical direction in the transformed image. Negative values represent negative frequencies and are located in the upper half plane, since this corresponds exactly to the coordinate system of fields, where the y-coordinate increases from top to bottom. With this orientation, the frequencies of a parallel fringe system are located along a line through zero frequency, perpendicular to fringes (37).

ii) Filtered Back-FFT to 2D Mod 2Pi Data

Back transformation with a Fast Fourier algorithm is applied to an active frequency window with a filter mask. In order to obtain modulo 2π phase data that correspond to intensity distribution of the forward-transformed interferogram, the mask covers all frequencies outside of the first order of the interferogram's frequency domain in only one of the quadrants (using the second order leads to unwrapped phase multiplied by two). Before backtransformation is computed, all masked complex amplitudes are set to zero and only unmasked data contributes to modulo 2π phase data (37).

iii)Unwrap with DCT

The problem of phase unwrapping can be met by solving Poisson equation with a specific form of the fast discrete cosine transform (DCT) (38). This approach is numerically stable, computationally efficient, and solves exactly Poisson's equation with proper boundary conditions. Local pixel phase difference (in a 4-neighbour sense) should be identical in both the wrapped and unwrapped 2D-Data. The unwrapped solution $\Phi i,j$ is the one that minimizes

$$\sum_{i=0}^{M-2}\sum_{j=0}^{N-1}(\Phi_{i+1,j}-\Phi_{i,j}-\Delta_{i,j}^{x})^{2}+\sum_{i=0}^{M-1}\sum_{j=0}^{N-2}(\Phi_{i,j+1}-\Phi_{i,j}-\Delta_{i,j}^{y})^{2} \tag{3.1}$$

where the subscripts (i,j) refer to discrete pixel locations in (x,y) of 2D-Data size $M \times N$ pixels. The phase-differences $\Delta_{i,j}$ from the original wrapped-phase data $\Psi_{i,j}$ in the horizontal direction x and the vertical direction y are

$$\Delta_{i,j}^{x}=W(\Psi_{i+1,j}-\Psi_{i,j}),\quad i=0,\dots,M-2,\qquad j=0,\dots,N-1$$

$$\Delta_{i,j}^{y}=W(\Psi_{i,j+1}-\Psi_{i,j}),\quad i=0,\dots,M-1,\qquad j=0,\dots,N-2$$

and 0 otherwise. W denotes an operator that wraps all values of its argument into the range $(-\pi,\pi)$. The normal equation that leads to the least-squares phase unwrapping solution can be written as (39)

$$\left(\Phi_{i+1,j}-2\Phi_{i,j}+\Phi_{i-1,j}\right)+\left(\Phi_{i,j+1}-2\Phi_{i,j}+\Phi_{i,j-1}\right)=\rho_{i,j} \tag{3.2}$$

where $\rho_{i,j}=\left(\Delta_{i,j}^{x}-\Delta_{i-1,j}^{x}\right)+\left(\Delta_{i,j}^{y}-\Delta_{i,j-1}^{y}\right)$. These equations relate wrapped- and unwrapped-phase differences in a discrete, 2D grid form of the Poisson equation

$$\frac{\partial^{2}}{\partial x^{2}}\Phi(x,y)+\frac{\partial^{2}}{\partial y^{2}}\Phi(x,y)=\rho(x,y) \tag{3.3}$$

with Neumann boundary conditions: $\nabla\Phi\cdot n=0$, which may be solved by the 2D DCT (40). The exact solution in the DCT domain is

$$\hat{\Phi}_{i,j} = \frac{\hat{\rho}_{i,j}}{2(cos\left(\frac{\pi i}{M}\right) + cos\left(\frac{\pi j}{N}\right) - 2)} \tag{3.4}$$

The unwrapped phase values $\Phi_{i,j}$ can then be obtained by performing the inverse DCT of Eq. *(3.4)* (37).

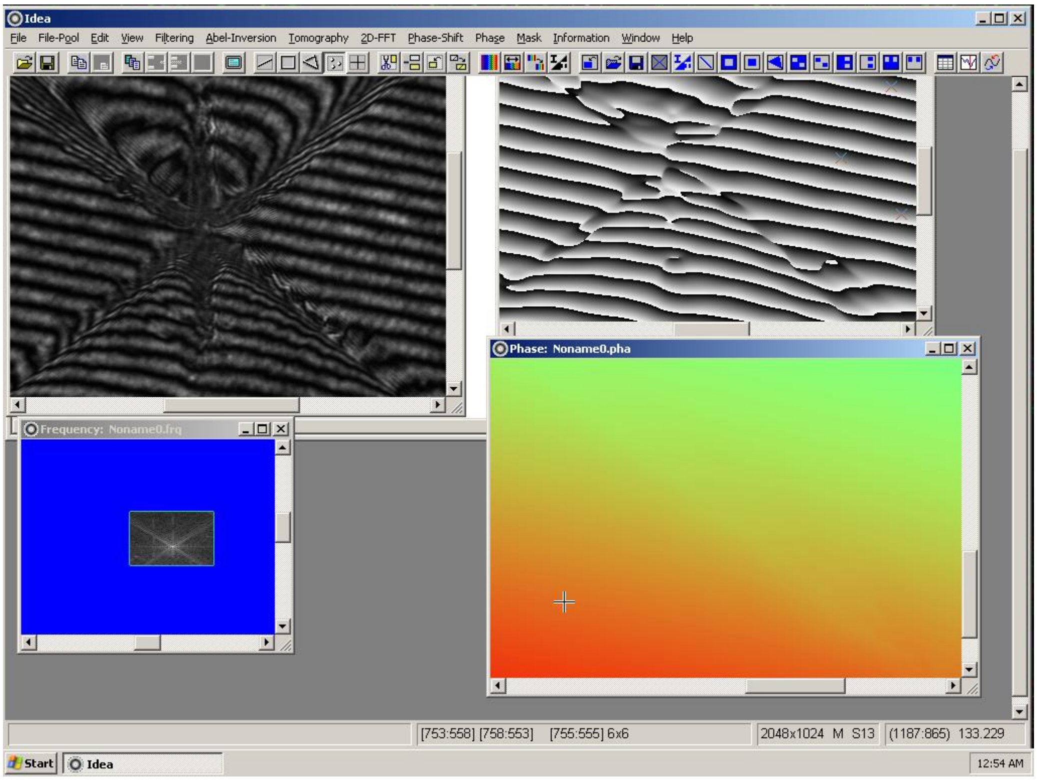

Figure 3.3: Illustration of the procedure for the signal image (on right corner is the phase shift before the subtracting).

For an image that has random defects alongside with the signal, the removal of these defects is a difficult process. However, if an image with the same defects is available, it is easy to subtract the image with the defects from the image with the signal and obtain the net signal. Thus, the same procedure is applied for the reference images.

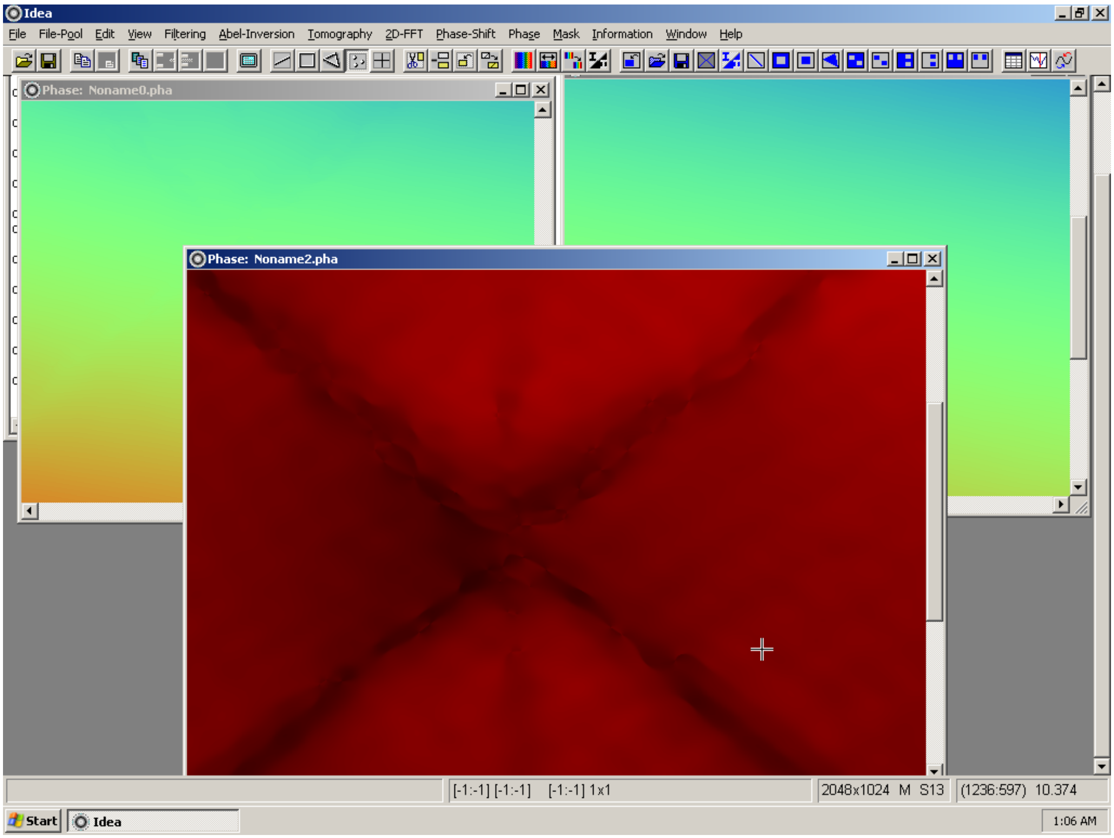

Figure 3.4: Illustration of the phase shift after subtracting the references phase from the signals phase.

3.1.3 Density Analysis

The radial distribution of the plasma density is obtained by applying Abel inversion transformation on the integral data of the phase shift image. Assume that an observer (I) looks along a line parallel to the x-axis a distance y above the origin. What the observer sees is the projection (i.e. the integral) of the circularly symmetric function $f(r)$ along the line of sight. The function $f(r)$ is represented in gray in the following figure. The observer is assumed to be located infinitely far from the origin so that the limits of integration are $\pm\infty$.

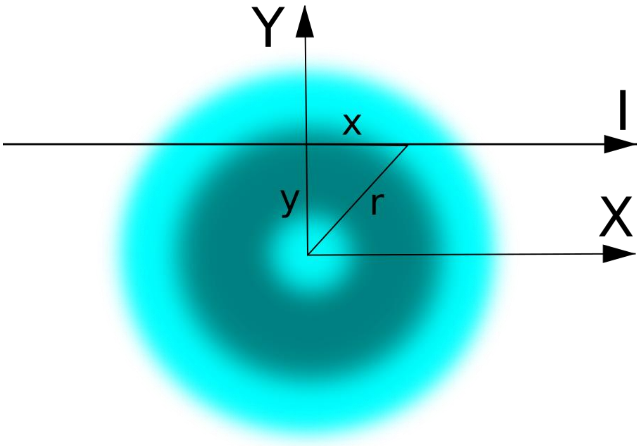

Figure 3.5: A geometrical interpretation of the Abel transform in two dimensions.

By assuming cylindrical symmetry of the plasma column, we proceed to Abel inversion transformation. The relation between integral data $h(y)$ and radial distribution $f(r)$ is given by the forward Abel Transform (37):

$$h(y) = 2\int_{y}^{R} f(r)\frac{r}{\sqrt{r^2 - y^2}}dr \tag{3.5}$$

where $h(y)$ is the integral phase shift. The radial distribution $f(r)$ from the integral is obtained by the Abel Inversion:

$$f(r) = -\frac{1}{\pi}\int_{y}^{R}\frac{dh(y)}{dy}\frac{dy}{\sqrt{r^2 - y^2}}dr \tag{3.6}$$

3.2 Experimental Results

3.2.1 Phase shift and density distribution

In order to understand the dynamics of the X-pinch plasma, a number of experiments were conducted in the laboratory and their results will be discussed at this paragraph.

The following shadowgraphs illustrate the time-evolution of the experiment:

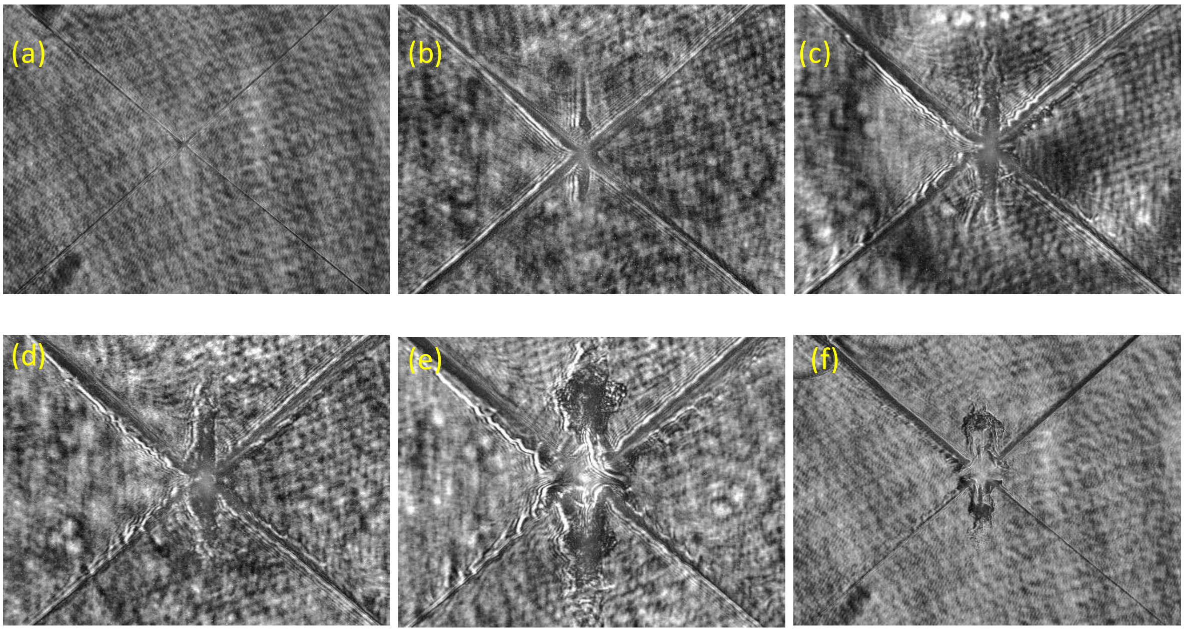

Figure 3.6: Shadowgraphs in times (a) 11ns (b) 19ns (c) 37ns (d) 42ns (e) 71ns (f) 78ns.

The first image (a) illustrates a very early state, where the coronal plasma begins to form but it is not very clear yet. On the second image (b) the wires have been expanded and the coronal plasma has already been formed as well as the plasma jets. On the third image (c) the neck starts to form due to the $m = 0$ instability, while the formation of the Rayleigh–Taylor instability across the wires is also observable. At the next stage (d) the neck has been compressed so much, due to the B field leading to hotspots formation and X-ray bursts coming from these regions. The mini-diode has already been formed on the (e) image. The long e-beam follows the path from the cathode to the anode through the mini-diode, which has been formed due to the collapse of the neck. Also X-ray bursts coming from this area. The last stage (f) is the final stage where the plasma begins to collapse.

The following shadowgraphs illustrate the time-evolution of the side view experiment:

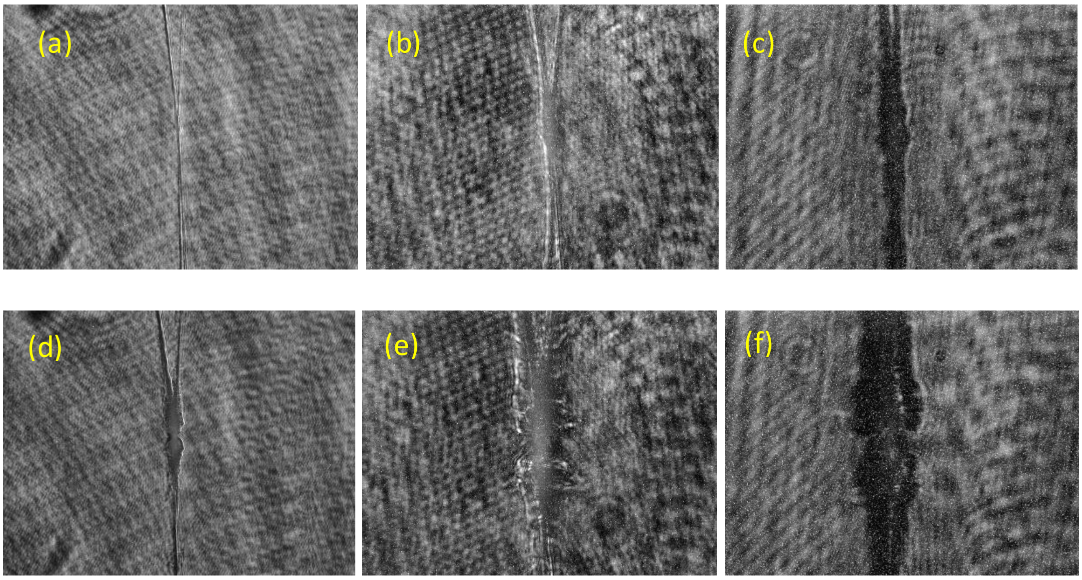

Figure 3.7: Side view shadowgraphs (a) 10 ns (b) 18 ns (c) 24.2 ns (d) 47.7 ns (e) 53.4 ns and (f) 60 ns after the current start.

The side view experiments were performed to depict the cylindrical deposition of plasma in order to perform the Abel inversion transform to obtain the density distribution of the X point. Unfortunately for times after 47 ns, is impossible to obtain the density distribution because of the pinch formation. The cylindrical deposition of the plasma in this area is no longer valid so the Abel inversion gives wrong results. Generally, in X-pinch it is difficult to calculate the density of plasma due to the requirements of the Abel inversion transform. This is the reason why this technique was not applied at the plasma jets. Although we assume that they have a cylindrical distribution, and in theory Abel inversion could be applied, the plasma bursts from the wires prevents us from doing this.

In order to calculate the phase shift and the plasma density distribution, the following interferograms were used. The selected interferograms cover the entire time range of the experiment.

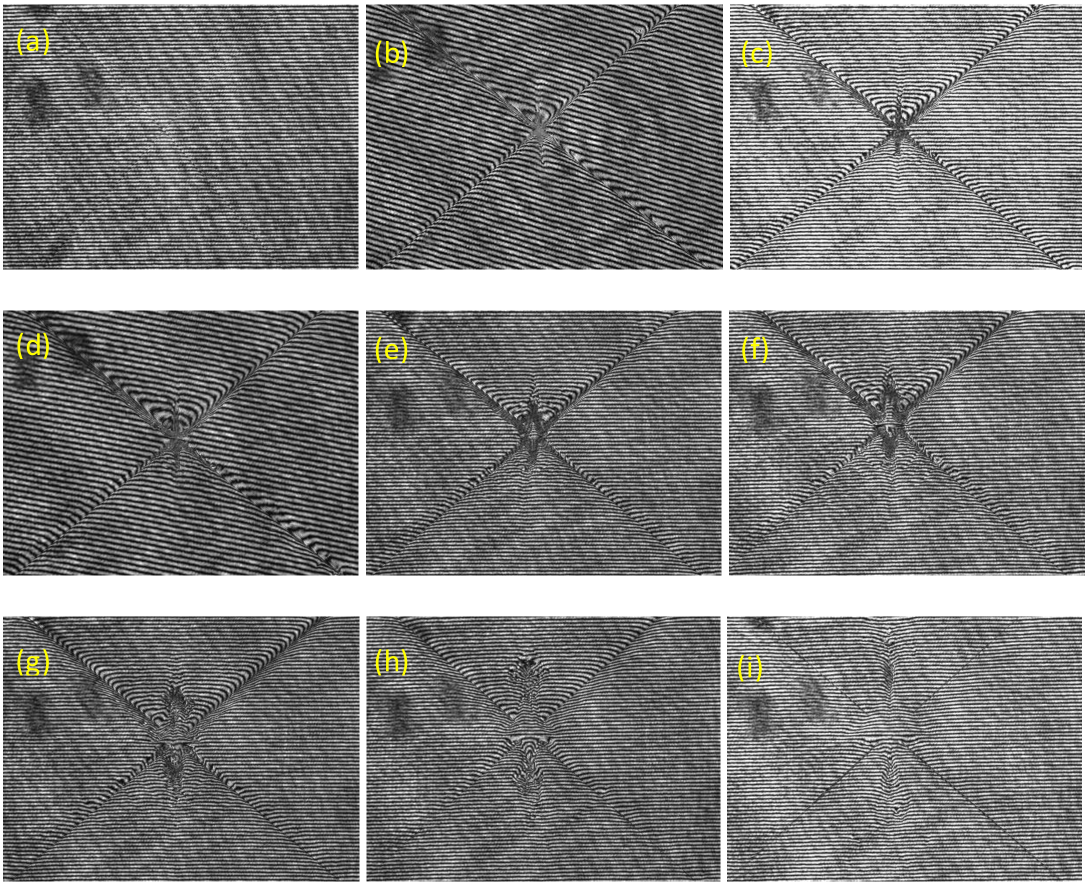

Figure 3.8: Interferograms (a) 1.6 ns (b) 28 ns (c) 37 ns (d) 39 ns (e) 47 ns (f) 55 ns (g) 71 ns (h) 90 ns (i) 123 ns after the current start.

The same procedure has been performed for the side view interferograms which are illustrated below.

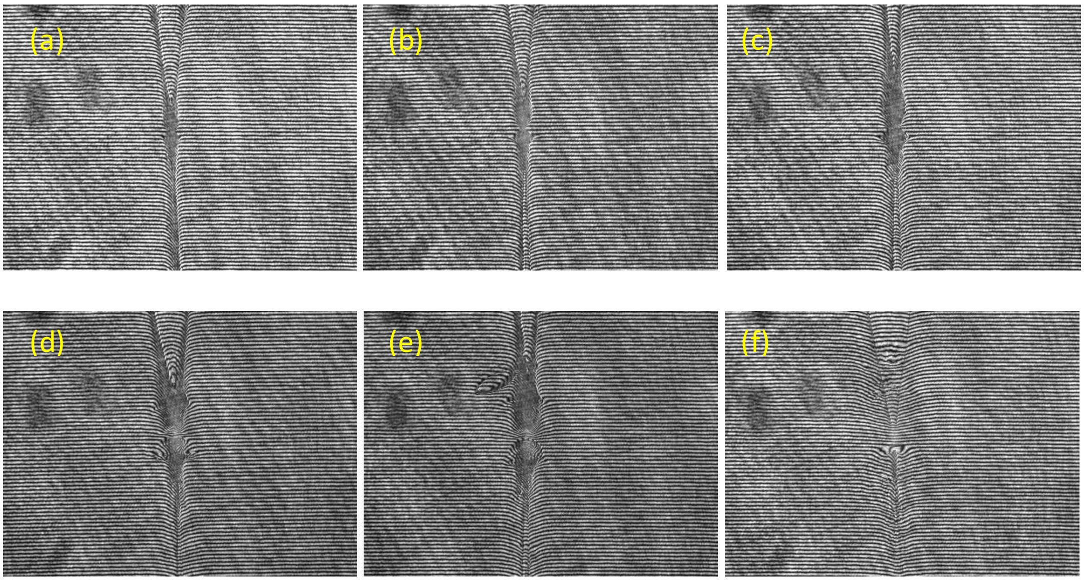

Figure 3.9: Side view of the Interferograms (a) 26 ns (b) 37 ns (c) 48 ns (d) 59 ns (e) 62 ns (f) 103 ns after the current start.

The figures 3.10-18 illustrate the unwrapped phase as calculated from the interferograms and the average density distribution at the X region. The light background stands for the unperturbed regions, where the laser beam passes through without phase shifting. However, the darker areas represent regions where the beam is subjected to phase shift, due to the presence of plasma.

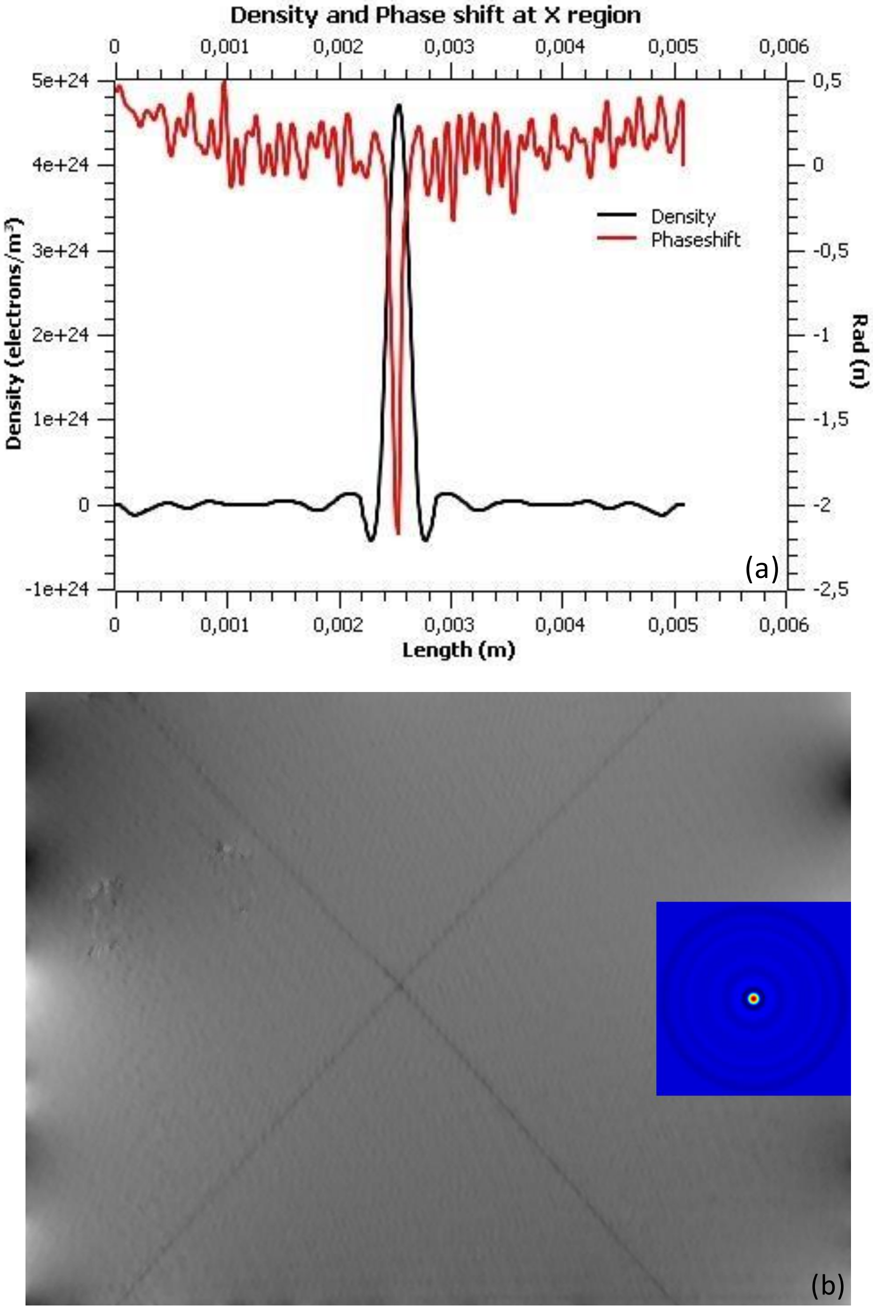

Figure 3.10: a) Phase shift and density distribution graph for 6 mm at the X point, 1.6 ns after the current start. b) Phase shift image. The insert depicts the radial density distribution around the X point.

For 1.6 ns, we have not received a corresponding side view experiment. We observe the density very concentrated since the experiment is in very early state.

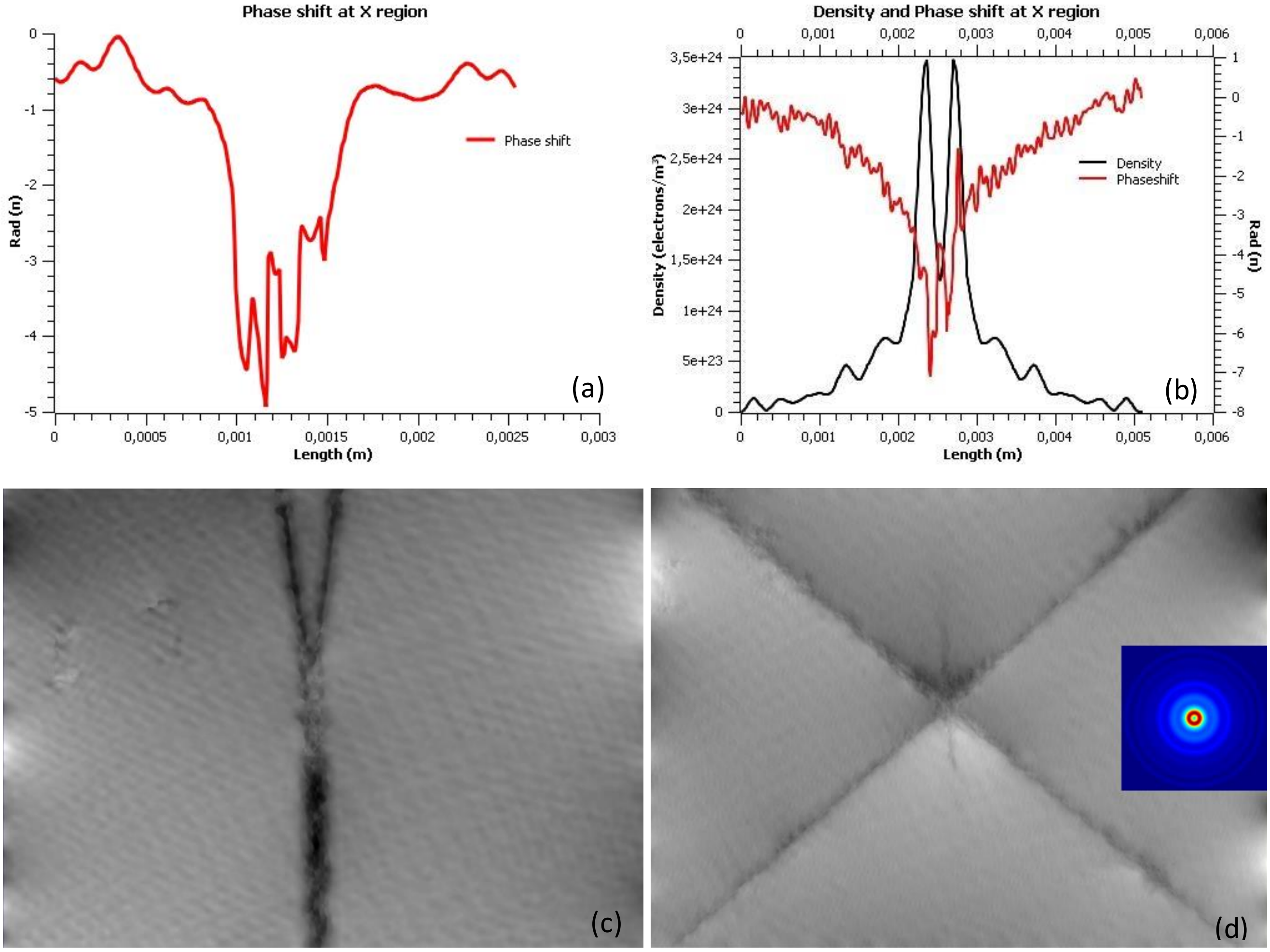

Figure 3.11: a) Phase shift graph for 3 mm at the X point (side view), 26 ns after the current start. b) Phase shift and density distribution graph for 6 mm at the X point (straight view), 28 ns after the current start. c) Phase shift image side view. d) Phase shift image straight view. (The insert illustrates the radial density distribution around X).

At this time the plasma is still in an early state. The cylindrical symmetry is valid and the maximum density is calculated at $3.5\text{x}10^{24}$ electrons per cubic meter. The plasma diameter at point X is about 1 mm.

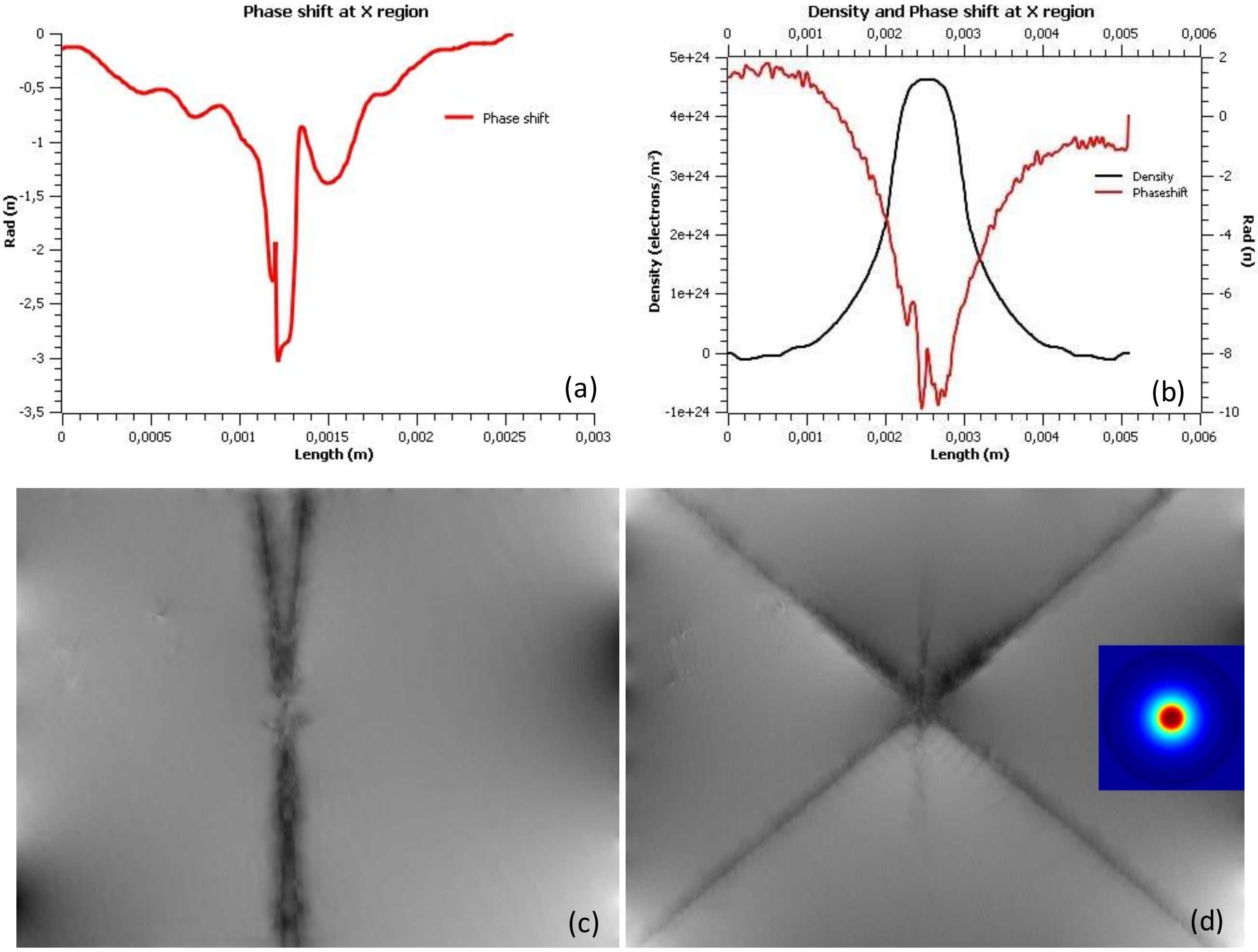

Figure 3.12: a) Phase shift graph for 3 mm at the X point (side view), 37 ns after the current start. b) Phase shift and density distribution graph for 6 mm at the X point (straight view), 37 ns after the current start. c) Phase shift image side view. d) Phase shift image straight view. The insert illustrates the radial density distribution around X.

In this experiment a maximum plasma density of $4.7\text{x}10^{24}$ electrons per cubic meter was observed at the X point. We notice that as the experiment progresses over time, the magnetic pressure increases in this region and the matter is getting denser at this point. The plasma diameter at point X is about 1.6 mm.

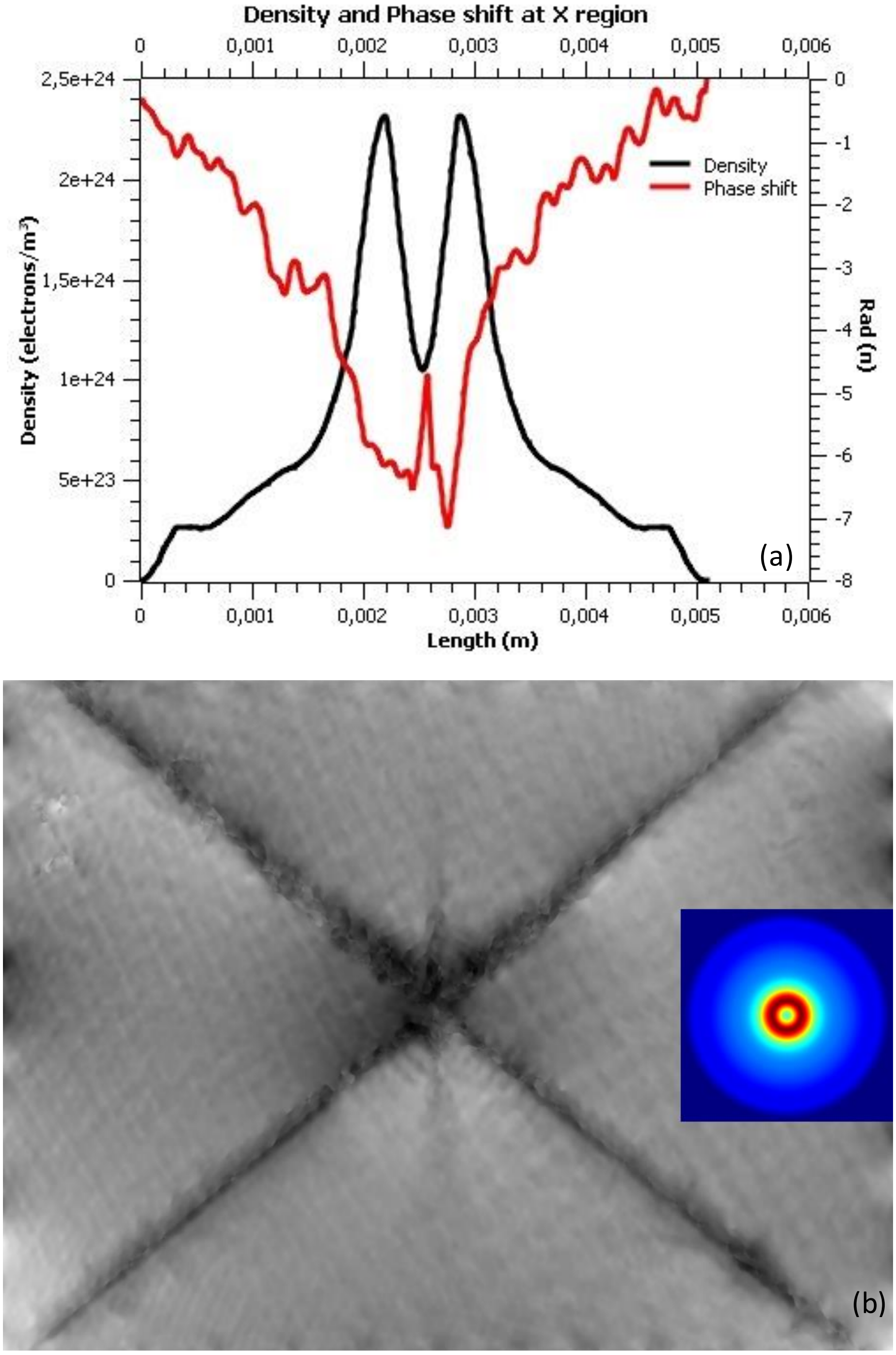

Figure 3.13: a) Phase shift and density distribution graph for 6 mm at the X point, 39 ns after the current start. b) Phase shift image. The insert depicts the radial density distribution around the X point.

Marginally yet we can measure the density in $2.4 \mathrm{x} 10^{24}$ electrons per cubic meter. For times after than the 39ns it is impossible to draw a conclusion about density, as the cylindrical symmetry breaks.

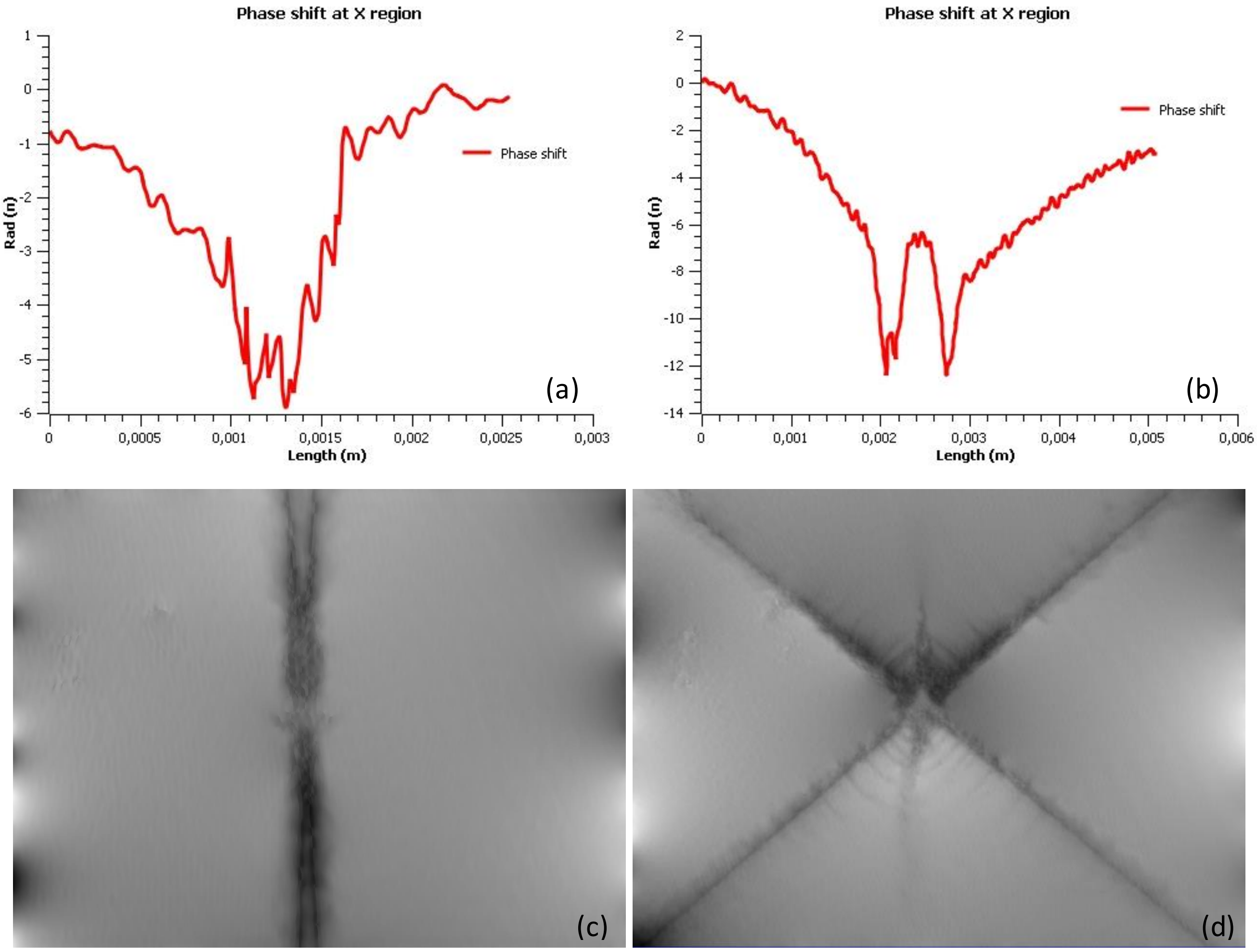

Figure 3.14: a) Phase shift for 3 mm at the X point (side view), 48 ns after the current start. b) Phase shift for 6 mm at the X point (straight view), 47 ns after the current start. c) Phase shift side view. d) Phase shift straight view.

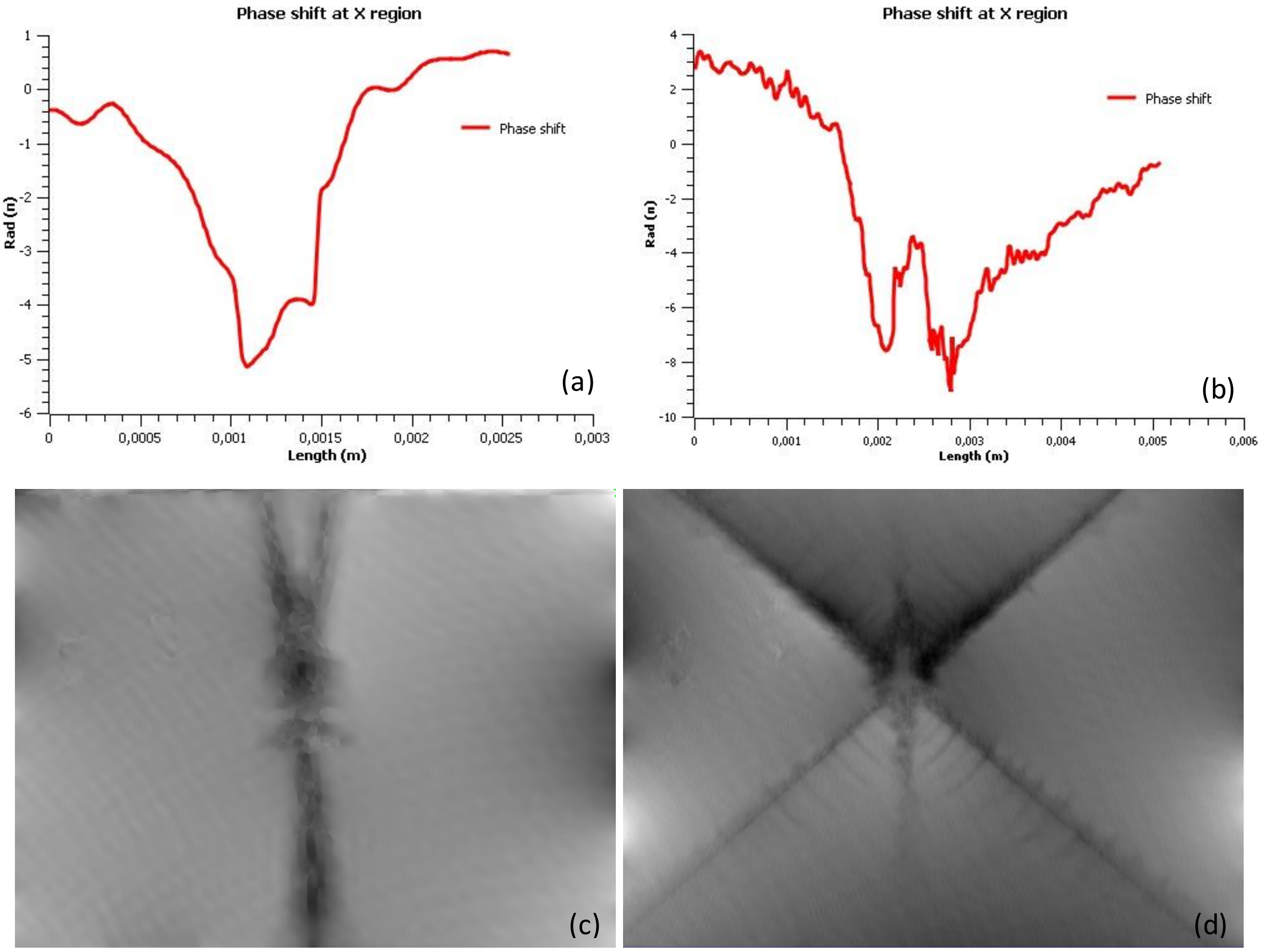

Figure 3.15: a) Phase shift graph for 3 mm at the X point (side view), 59 ns after the current start. b) Phase shift graph for 6 mm at the X point (straight view), 55 ns after the current start. c) Phase shift image side view. d) Phase shift image straight view.

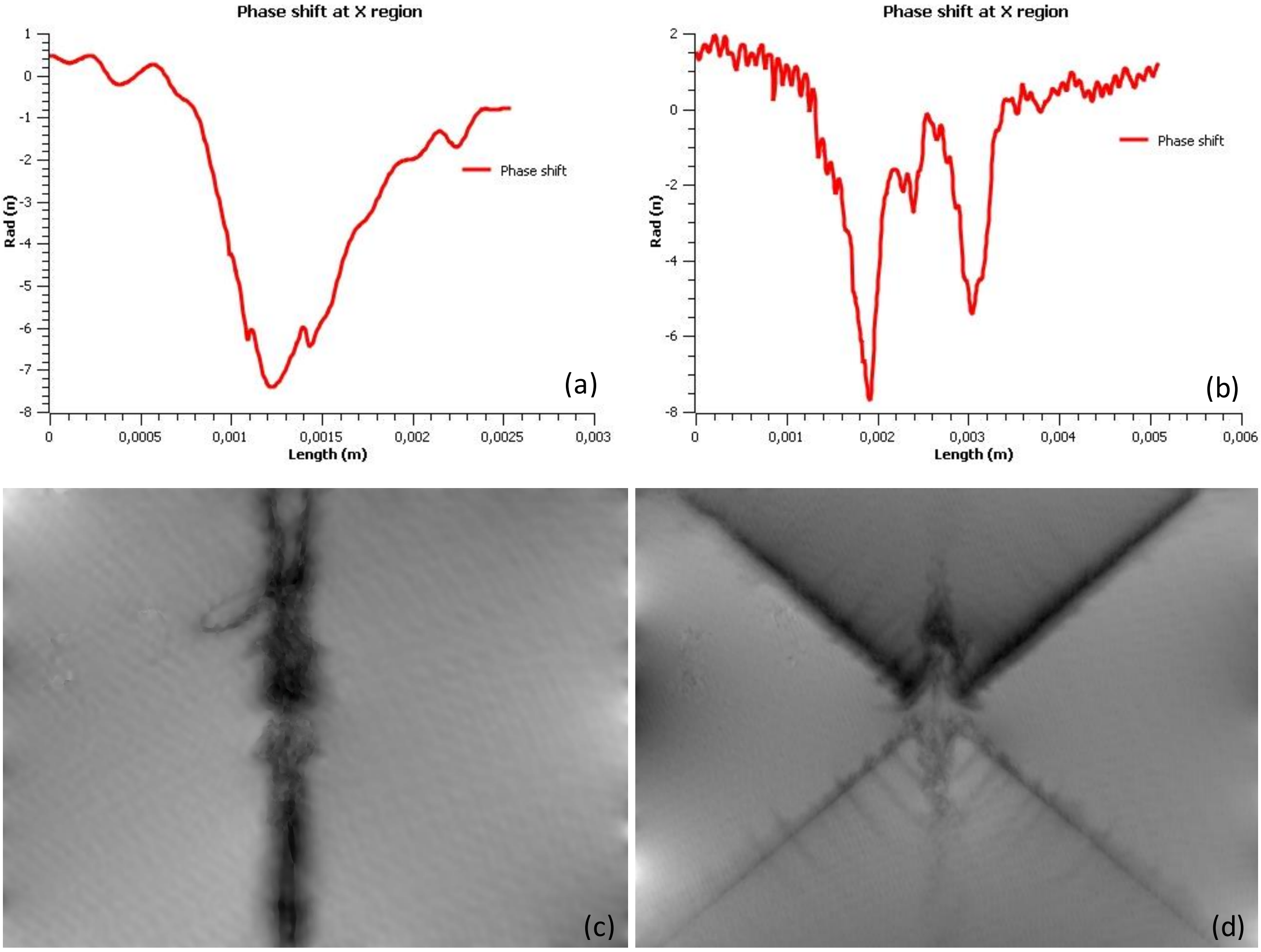

Figure 3.16: a) Phase shift graph for 3 mm at the X point (side view), 62 ns after the current start. b) Phase shift graph for 6 mm at the X point (straight view), 71 ns after the current start. c) Phase shift image side view. d) Phase shift image straight view.

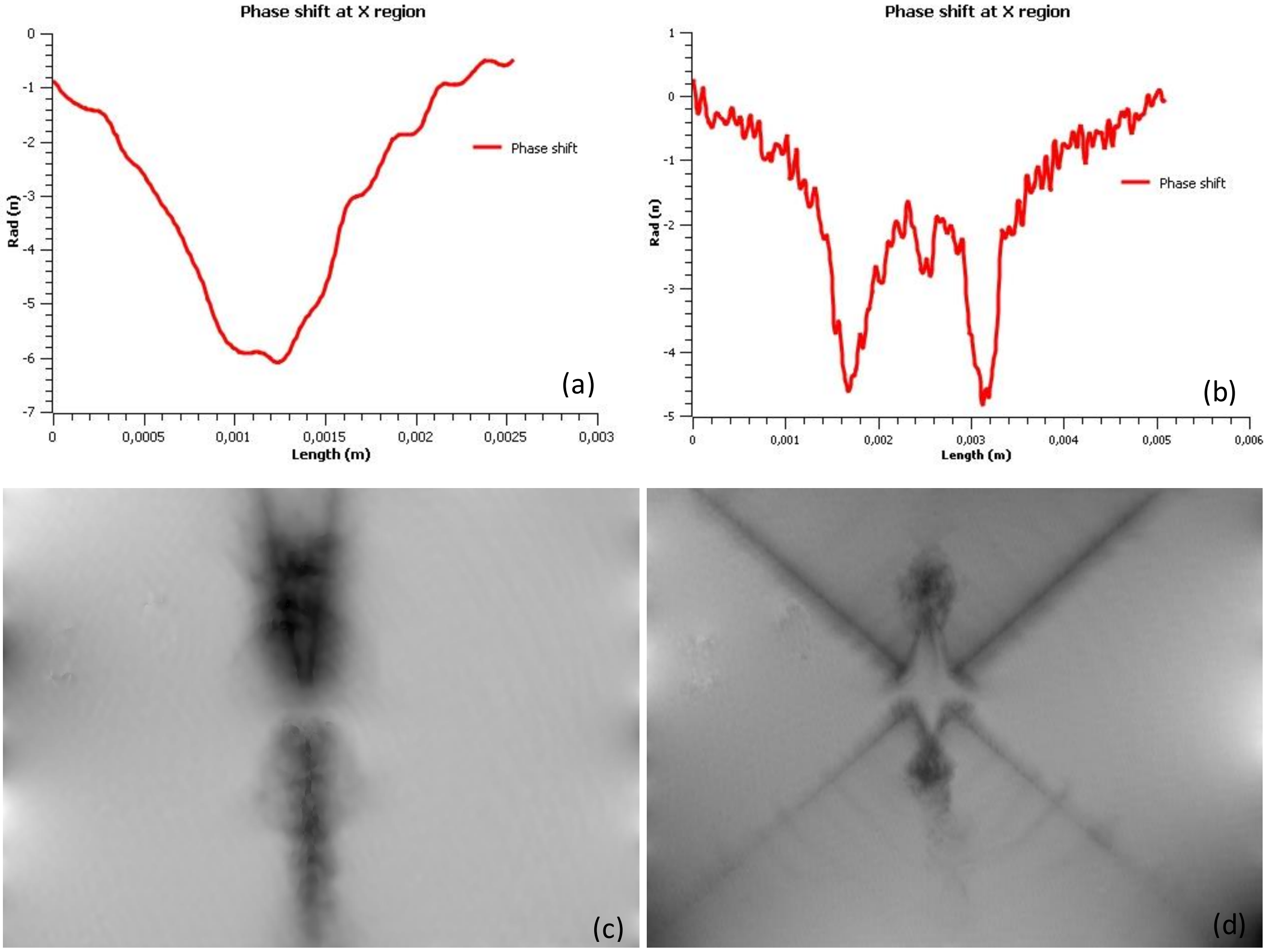

Figure 3.17: a) Phase shift graph for 3 mm at the X point (side view), 103 ns after the current start. b) Phase shift graph for 6 mm at the X point (straight view), 90 ns after the current start. c) Phase shift image side view. d) Phase shift image straight view.

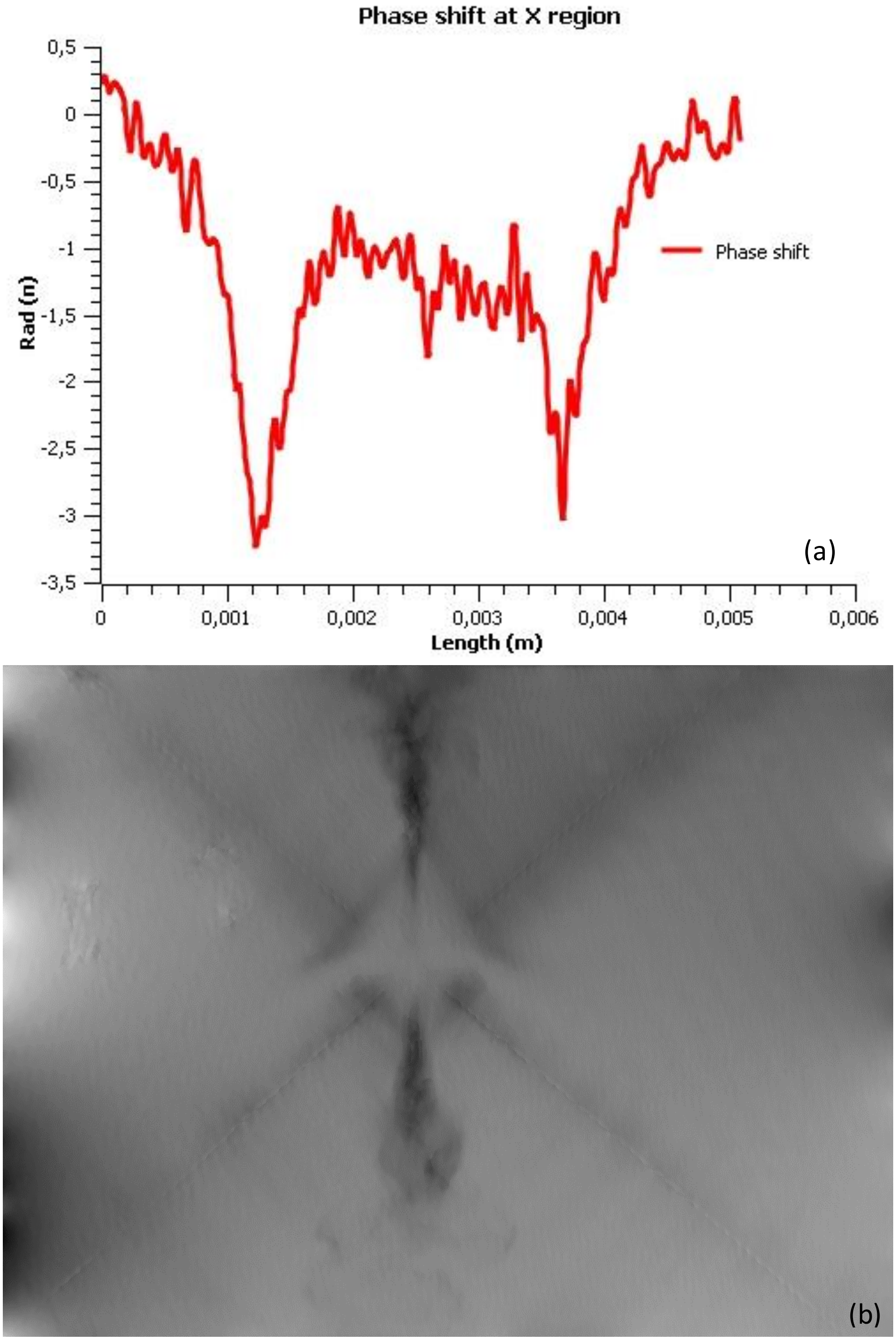

Figure 3.18: a) Phase shift and density distribution graph for 6 mm at the X point, 123 ns after the current start. b) Phase shift image.

A large phase shifting of the laser beam was observed in high density plasma areas. Specifically, the phase shift at 48 ns (about at the current peak), reached -12π at the X region. The phase shifting decreases for later times. The deviations in the measured values between the side view and straight view experiments are due to the fact that the measurements were not taken exactly at the same spatial and temporal points.

3.2.2 X-ray production

The figures below illustrate the X-ray production mechanism. The plasma column collapses on itself in one or more spots along the column (often referred to as “hot spots” or micro-pinches). A burst of X-rays is emitted from each of the hotspots, and shortly after X-ray emission a small gap opens up, across which electrons are accelerated.

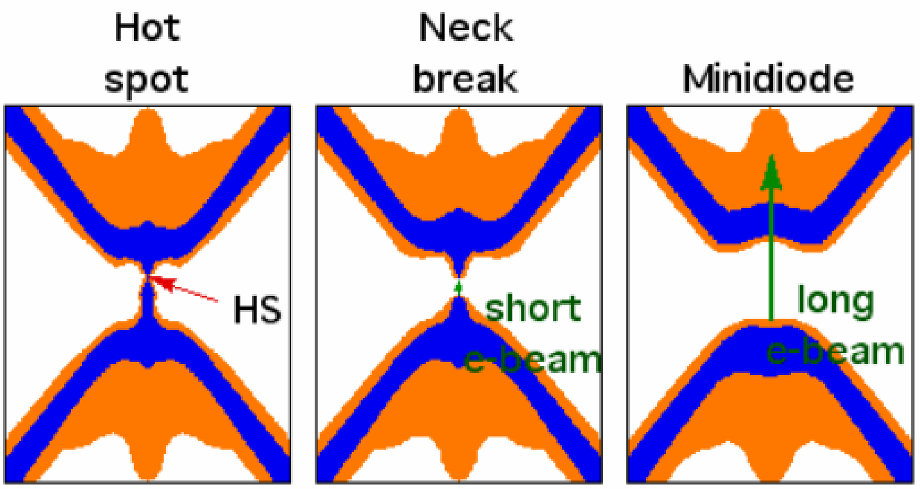

Figure 3.19: X-ray production mechanism in an X-pinch (27).

The following diagram depicts the emission line Lg1 11 keV (the burst that captured by the photomultiplier (PMT) and the photodiode (PD) at the same time), as the radiation was strong enough to escape from the vacuum chamber and be recorded by the PMT but also was within the bandwidth of the photodiode (cut-off ~10KeV). The second burst that captured only by the PMT was one of the K lines (59 keV, 57 keV or 67 keV), as it was beyond the bandwidth of the photodiode. The pulse duration for the K line emission was 3.1 ns and for L line was 3.7 ns.

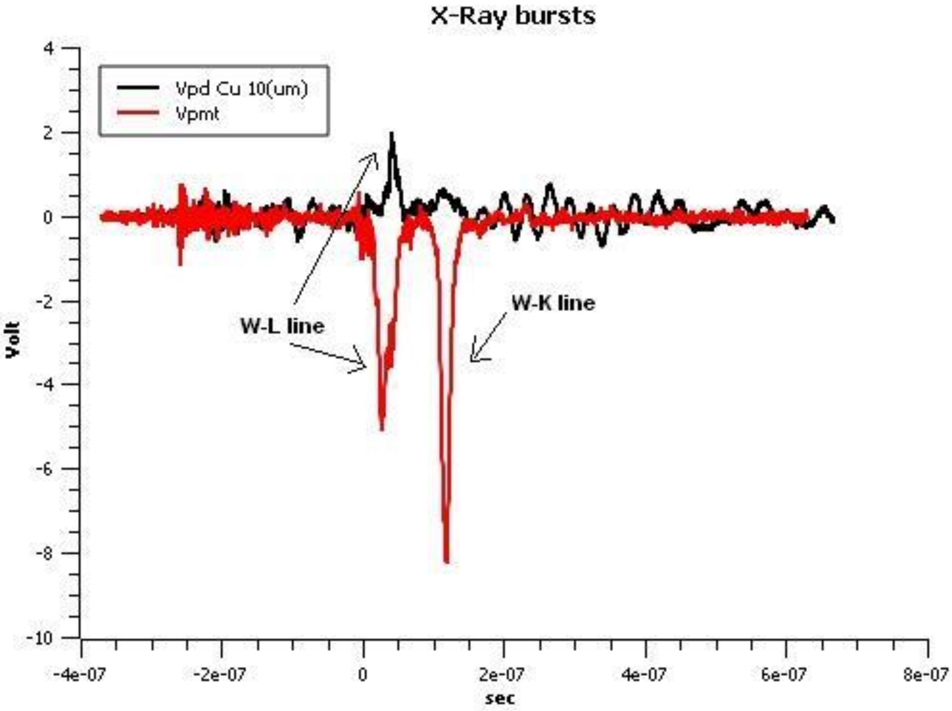

Figure 3.20: Signals from PD Cu (10 um) and PMT.

At the figure below the same signal has been captured from the PD Al (10 um) and the PD Ti (15 um). The difference in transmission response for the particular energy range for the two filters leads us to the conclusion that it is the Lg1 11 keV emission line.

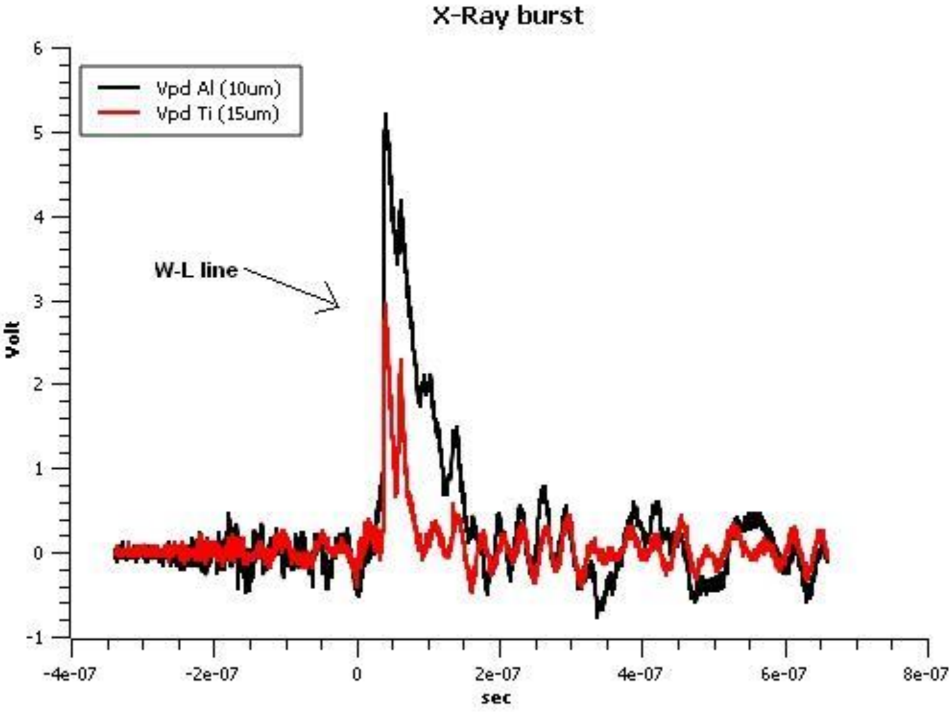

Figure 3.21: Signals from PD Al (10 um) and PD Ti (15 um)

The 9.6 keV emission line has been captured from the PD Al (10 um) and the PD Cu (10 um). The specific difference in transmission response of the PD covered with aluminum filter in relation to the PD covered with copper filter indicates that it is the Lb1 emission line.

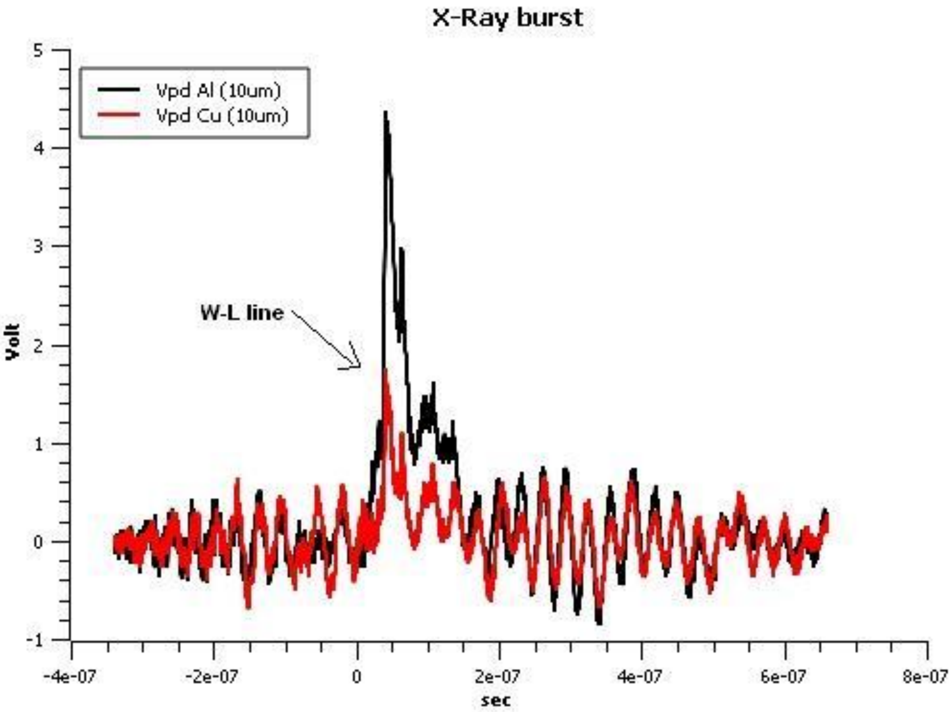

Figure 3.22: Signals from PD Al (10 um) and PD Cu (10 um).

The figure 3.23 depicts SXR bursts captured by the PD, while the PMT did not record any signal. This is the result of low plasma dynamics. The current is not strong enough to extract the K emission lines of the tungsten. In this case, can have been recorded any of the L lines with pulse duration 4 ns except of the Lg1. The following shadowgraphs (figure 3.24) correspond to the referred capture.

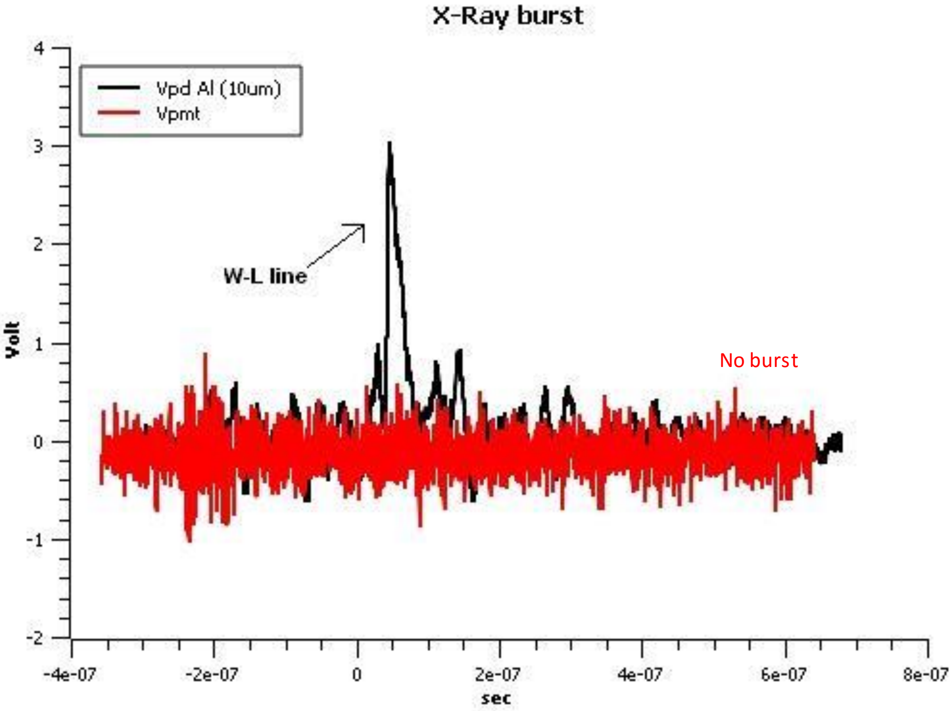

Figure 3.23: Signals from PD Al (10 um) and from PMT.

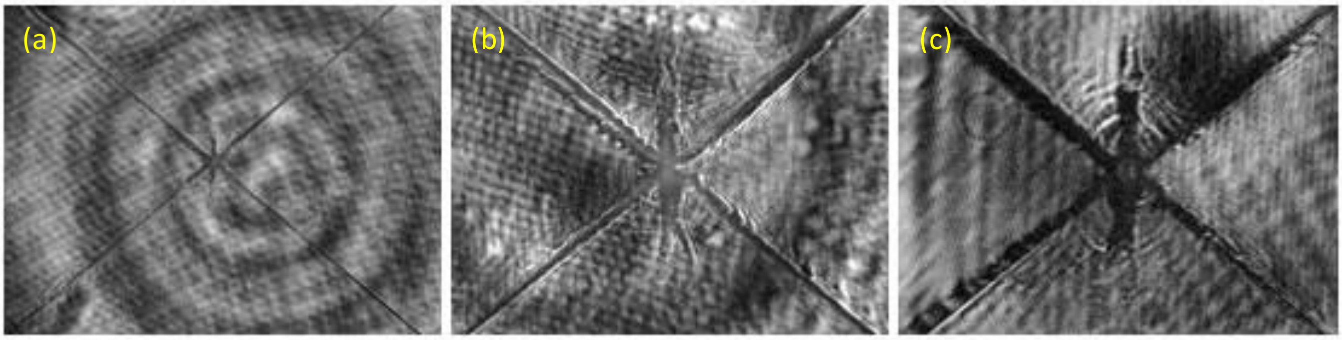

Figure 3.24: (a) 29 ns, (b) 37 ns and (c) 43 ns after the current start.

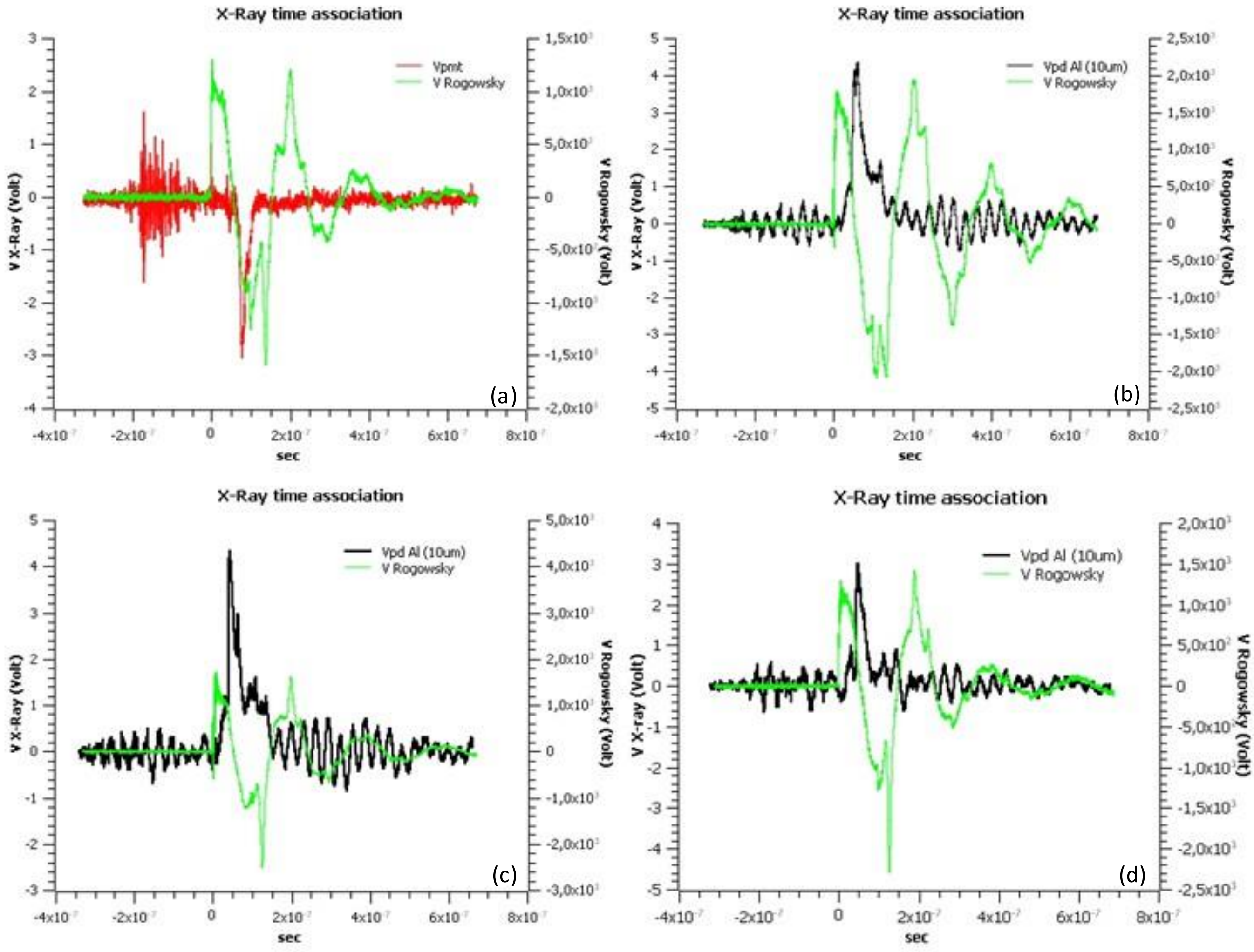

Figure 3.25: X-ray time association

As shown in the above figures, the X-ray bursts occurs in times (a) 70ns, (b) 50ns, (c) 40ns and (d) 40ns. Notice that the emissions occur after the current peak i.e. at pinch times. In conclusion, the radiation bursts have a good time sequence between the experiments with an average time 50ns after the current start.

3.2.3 Jets expansion velocity

The calculation of the plasma jets expansion velocity was performed using six consecutive images of two selected experiments for times before and after the pinch stage. The image from the (a) Pike camera has a field frame 8.14 mm and the (b), (c) Guppy cameras have 4.13 mm. By knowing the cameras field frames and counting the interference fringes that are shown in each image, the physical distance between two fringes was calculated. In order to find out the region occupied by the plasma jets on each image, was calculated the physical distance of the perturbation by counting the perturbed fringes and multiply them with the distance between two fringes. The mean velocity of the plasma jets was found by subtracting the perturbed area between two images and divided by the time difference between them.

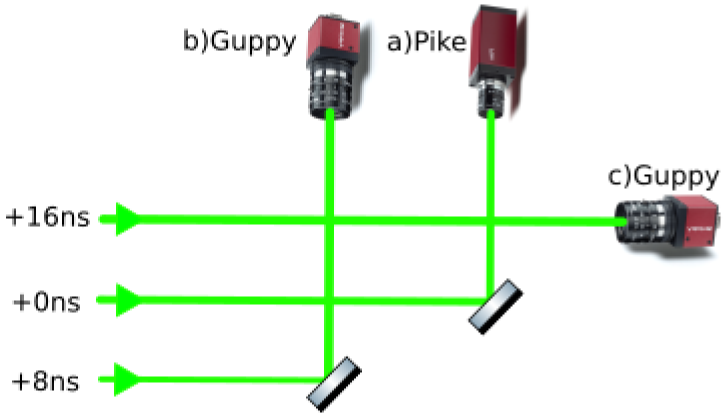

Figure 3.26: CCD Cameras layout

The images were analyzed at times (a) 1.64 ns, (b) 9.44 ns, (c) 15.94 ns, (d) 37.04 ns, (e) 44.84 ns and (f) 51.34 ns after the current start and are presented in figure 3.27.

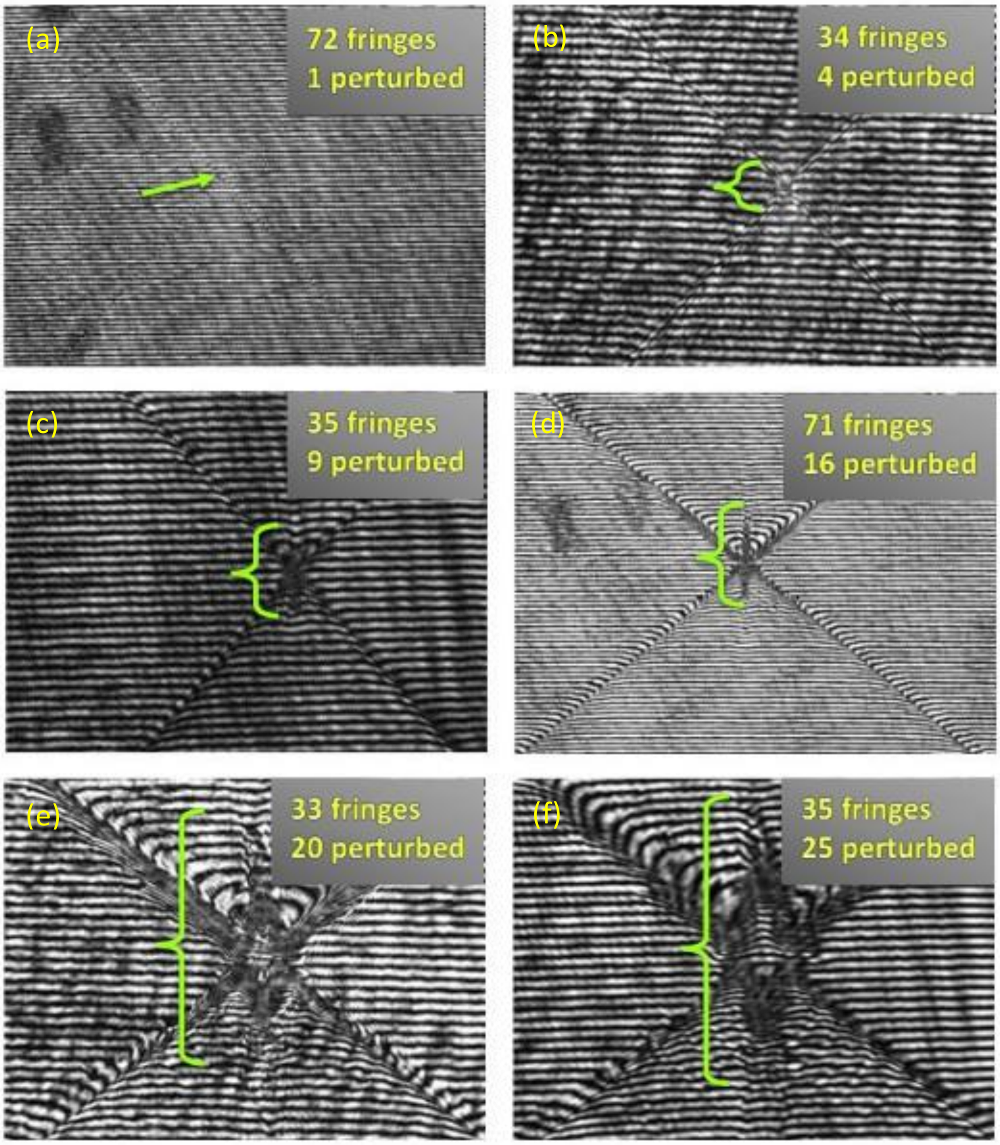

Figure 3.27: Interferograms at times (a) 1.64 ns, (b) 9.44 ns, (c) 15.94 ns, (d) 37.04 ns, (e) 44.84 ns and (f) 51.34 ns after the current start.

It was calculated that from 1.64 ns to 9.44 ns the plasma jets expands with a mean velocity 53000 m/sec in both directions. The same procedure was followed for the time windows: 9.44 ns to 15.94 ns, 15.94 ns to 37.04 ns, 37.04 ns to 44.84 ns and 44.84 ns to 51.34 ns. The mean expansion velocities were found to be 82000 m/sec 110338 m/sec, 95500 m/sec and 63800 m/sec for each case respectively.

It seems that the results follow a normal distribution just as expected. If we compare the expansion speeds with the corresponding images it is observed that the maximum mean expansion velocity is recorded in the time window just before the pinch. At this time the magnetic pressure is in the maximum value around the cross point, forcing the plasma jets to accelerate at enormous velocities (32).

Chapter 4: Conclusions and Future work

In this thesis experiments designed to study the dynamics of the X pinch were presented, studied and analyzed. From the analysis of the experimental results, the main conclusions can be summarized as follows:

- The density measured was of the order of magnitude of 10^{24} electrons per cubic meter at the X region.
- The plasma jet mean speeds were observed up to 110,338 Km/sec.
- High energy X-ray radiation (K, L lines) having an emission duration as short as 3.1-4.0 ns was measured.

In summary, such devices can provide very focused X-ray sources with high-intensity.

There are many options on the expansion of this research and improvement of the understanding of the X-pinch dynamics.

- More data on various wire materials, wire diameters, current shapes, and X-pinch geometries will give valuable information about the physical mechanisms that dominate X-pinch dynamics.
- We were limited in our experiment by the 532 nm wavelength of the laser light. The peak densities and density gradients were too high during the current pulse for the laser to penetrate the plasma. Higher energy photons could be used to resolve these areas.
- Further studies are needed to develop the X-pinch as a convenient laboratory and bio-medical imaging source. The X-pinch mechanisms are challenging as a high resolution (both temporal and spatial) imaging source. However, in order to make the X-pinch useful to a broader user base it must be reliable and well characterized. The X-pinch needs to be optimized to get the best imaging characteristics out of the small amount to energy. This would downgrade the requirements of the pulsed power source and would allow for more compact designs. It is important to continue the research in order to find ways to control the radiation characteristics and increase the repetition rate on X-ray pulses.

Annex

The jets velocity calculations are performed by the following simple code written in Mathematica, whereas fringes1, fringes2, n1 and n2 we define the total counted fringes and the perturbed fringes of each image. To perform the analysis of the image captured from the first camera we change the value of frame1 to $8.14\text{x}10^{-3}$:

```
fringes1 = ;
n1 = ;
frame1 = 4.13*10^-3;
fringes2 = ;
n2 = ;
frame2 = 4.13*10^-3;
t = 7*10^-9;
x1 = frame1/fringes1;
x2 = frame2/fringes2;
x = (x2*n2) - (x1*n1);
u = x/t
```

At the following table is presented the time data from all the experiments that performed in the context of this thesis.

a/a	date	experiment	current peak time (ns)	current peak value (uV s)	filter	2nd filter	1st PD time relative to current start (ns)	2nd PD time relative to current start (ns)	PMT time relative to current start (ns)	1st PD value (V)	2nd PD value (V)	PMT value (V)
1	29 July 2016, 11:21:45 am	interf	57	43,5	Al-10um	-	45,3054	-	26,945	4	-	4
2	29 July 2016, 12:18:09 pm	shadow	55,7	40	Al-10um	-	49,9054	-	31,945	3.3	-	6.3
3	29 July 2016, 05:36:44 pm	interf	55,7	39,1	Al-10um	-	59,3054	-	30,745	3.7	-	7.2
4	29 July 2016, 08:40:37 pm	interf	53,6	39,9	Al-10um	-	41,3054	-	26,445	2	-	5.1
5	29 July 2016, 01:28:21 pm	shadow	54	40,6	Al-10um	-	46,3054	-	-	3	-	-

6	29 July 2016, 06:16:40 pm	shadow	53,3	42,7	Al-10um	-	44,7054	-	32,545	3.3	-	6.5
7	29 July 2016, 06:53:23 pm	shadow	53,8	39,9	Al-10um	-	61,2054	-	32,345	2	-	4.2
8	29 July 2016, 07:38:35 pm	shadow	52,5	40	Al-10um	-	41,9054	-	34,545	2	-	4.7
9	29 July 2016, 08:00:44 pm	shadow	55	39	Al-10um	-	-	-	30,945	-	-	3
10	01 August 2016, 11:54:30 am	interf	53	41	Al-10um	-	50,9054	-	45,945	3	-	6.3
11	01 August 2016, 01:14:22 pm	shadow	54,7	42,7	Al-10um	-	49,3054	-	33,345	3.2	-	4.1

12	01 August 2016, 01:52:58 pm	shadow	53,7	46	Al-10um	-	52,3054	-	44,345	2.4	-	4.3
13	01 August 2016, 02:41:28 pm	shadow	52,7	45	Al-10um	-	46,4054	-	30,945	2.6	-	5.4
14	01 August 2016, 04:36:06 pm	interf	53,9	46	Ti-15um	Al-10um	43,9054	44,1054	-	2.9	3.8	-
15	01 August 2016, 05:22:20 pm	interf	53,2	43,6	Ti-15um	Al-10um	60,6054	41,3054	-	1.8	3.1	-
16	01 August 2016, 06:04:06 pm	interf	56	45	Ti-15um	Al-10um	44,9054	47,1054	-	2.7	4.9	-

17	01 August 2016, 07:06:04 pm	interf	53,4	47,6	Ti-15um	Al-10um	59,6054	59,3054	-	1.4	2.8	-
18	01 August 2016, 07:36:52 pm	interf	53,5	40	Ti-15um	Al-10um	46,3054	47,0054	-	3.3	5.2	-
19	02 August 2016, 10:44:20 am	interf	53,5	47	Ti-15um	Al-10um	44,3054	42,3054	-	1.3	2.7	-
20	02 August 2016, 12:00:38 pm	interf	55,8	51,5	Ti-15um	Al-10um	40,7054	40,9054	-	2.9	5.2	-
21	02 August 2016, 12:30:52 pm	interf	53,8	53,7	Ti-15um	Al-10um	41,3054	43,0054	-	2.6	5.1	-

22	02 August 2016, 12:56:22 pm	interf	56,8	48,9	Ti-15um	Al-10um	43,2054	43,8054	-	1.6	2.9	-
23	02 August 2016, 01:34:40 pm	interf	55,3	44,4	Ti-15um	Al-10um	51,1054	50,5054	-	1.4	3.3	-
24	02 August 2016, 01:51:54 pm	interf	54	48,7	Ti-15um	Al-10um	43,6054	43,2054	-	1.9	4	-
25	02 August 2016, 04:49:46 pm	interf	55,7	48	Cu-10um	Al-10um	-	49,6054	-	-	3.1	-
26	02 August 2016, 05:05:56 pm	interf	54,1	47,9	Cu-10um	Al-10um	49,1054	48,9054	-	0.6	1.4	-

27	02 August 2016, 05:58:56 pm	interf	54,6	51	Cu-10um	Al-10um	47,6054	53,6054	-	1.2	3.9	-
28	02 August 2016, 06:22:12 pm	interf	54,2	46	Cu-10um	Al-10um	45,6054	47,0054	-	2.3	5	-
29	02 August 2016, 07:03:06 pm	interf	96,6	25,3	Cu-10um	Al-10um	-	-	-	-	-	-
30	02 August 2016, 07:23:58 pm	interf	52,6	46	Cu-10um	Al-10um	41,9054	42,1054	-	1.7	4.3	-
31	02 August 2016, 07:44:26 pm	interf	54,2	51	Cu-10um	Al-10um	42,3054	50,0054	-	0.8	4.2	-

32	03 August 2016, 03:01:48 pm	interf	55,6	54,4	Cu-10um	Al-10um	52,3054	43,9054	-	1.1	3	-
33	03 August 2016, 03:22:44 pm	interf	96,6	33,9	Cu-10um	Al-10um	-	-	-	-	-	-
34	03 August 2016, 03:47:08 pm	interf	54	48	Cu-10um	Al-10um	46,3054	46,0054	-	2.3	5.3	-
35	03 August 2016, 04:22:44 pm	interf	52	48,3	Cu-10um	Al-10um	49,3054	49,6054	-	2.8	5.3	-
36	03 August 2016, 04:49:06 pm	interf	52,7	43,3	Cu-10um	Al-10um	47,5054	48,7054	-	1.9	4	-

37	03 August 2016, 05:11:52 pm	interf	51,5	46,5	Cu-10um	Al-10um	48,7054	48,9054	-	2.4	5.4	-
38	03 August 2016, 06:26:40 pm	interf	53,3	55,7	Cu-10um	Al-10um	-	42,3054	-	-	3.5	-
39	03 August 2016, 06:47:58 pm	interf	51,4	49,2	Cu-10um	Al-10um	50,6054	51,0054	-	2.1	4	-
40	03 August 2016, 07:16:38 pm	interf	52,8	60,4	Cu-10um	Al-10um	51,5054	52,1054	-	1.9	4.3	-
41	03 August 2016, 07:46:14 pm	interf	51,7	51,6	Cu-10um	Al-10um	50,7054	51,7054	-	1.4	3.9	-

42	04 August 2016, 10:24:38 pm	interf	52,5	47,1	Cu-10um	Al-10um	50,4054	50,4054	-	2.3	4.2	-
43	04 August 2016, 05:21:38 pm	interf	52,1	41,2	Cu-10um	Al-10um	63,5054	40,3054	-	2.2	3.9	-
44	04 August 2016, 05:43:18 pm	interf	54,4	44,6	Cu-10um	Al-10um	-	49,9054	-	-	1.8	-
45	04 August 2016, 06:03:04 pm	interf	55,6	45,8	Cu-10um	Al-10um	-	47,8054	-	-	2.7	-
46	04 August 2016, 06:42:02 pm	interf	52,9	51,5	Cu-10um	Al-10um	53,1054	44,9054	-	1.7	2.3	-

47	04 August 2016, 07:08:50 pm	interf	53,1	55,7	Cu-10um	Al-10um	49,7054	50,5054	-	1.4	3.8	-

table_annex 1: Experimental Data.

References – Bibliography

1. **Franklin R.N. and Braithwaite N.S.J.** *Plasma Sources.* s.l.: Sci. Technol. 18(7):010201, 2009.
2. **Langmuir Irving and Hugh Taylor.** *Biographical Memoirs of Fellows of the Royal Society.* s.l.: 4:167–184, 1958.
3. **Mott-Smith H.M.** *History of "plasmas".* Texas: Nature 233(219), 1971.
4. **Frank-Kamenezki D.A.** *Plasma Der Vierte Aggregatzustand.* 1963.
5. **Garcia Damien.** *Robust smoothing of gridded data in one and higher dimensions with missing values. Computational Statistics & Data Analysis.* s.l. : 54(4):1167 – 1178, 2010.
6. **Hutchinson I.H.** *"Principles of plasma diagnostics".* Cambridge: Cambridge University Press, 1987.
7. **Swanson D.G.** *Plasma Waves. 2nd edition.* 2003.
8. **Stix Thomas Howard.** *Waves in Plasmas.* 1992.
9. **Chen F. F.** *Introduction to plasma physics and controlled fusion.* New York: Plenum Press, 1974.
10. **Tatarakis M. et al.** Optical probing of fiber z-pinch plasmas. *Physics of Plasmas.* 5, 682, 1998.
11. **Merzkirch W.** *Flow visualization, page. 123–134.* Universitat Essen, Federal Republic of Germany: Academic Press, 1987.
12. **R. de Bruyn et al.** Apparatus for the study of Rayleigh–Bénard convection in gases under pressure. *Rev. Sci. Instrum.* 1996.
13. **E. Kaselouris et al.** Preliminary investigation on the use of low current pulsed power Z-pinch plasma devices for the study of early stage plasma instabilities. *Plasma Phys. Control. Fusion.* 2017.

14. **M. Van Marum.** Vancouver: AIP,Woodbury, NY, 1997. 4th International Conference on Dense Z-Pinches.
15. **J. A. Pollock and S. Barraclough.** 1905. Procession of the Royal Society NSW 39, 131.
16. **E. F. Northrup.** Some Newly Observed Manifestations of Forces in the Interior of an Electric Conductor. *American Physical Society.* 1907, Phys. Rev. 45, 890.
17. **W. H. Bennett.** Magnetically Self-Focussing Streams. *American Physical Society.* 1934, Phys. Rev. 45, 890.
18. **Dimitriou V. et al.** Studying the initial stages of plasma generation using ns laser pulsed systems and strong currents. *SPIE. OPTICS + OPTOELECTRONICS, Prague, Czech Republic.* 2015.
19. **Kaselouris E. et al.** Invited Talk: The influence of the solid to plasma phase transition on the generation of plasma instabilities. *44th EPS Conference on Plasma Physics, Belfast, Northern Ireland (UK).* 2017.
20. **Koundourakis G. et al.** Computational study of plasma dynamic evolution produced by low current table-top pinch plasma devices. *35th European Conference on Laser interaction with matter, Rethymno.* 2018.
21. **Skoulakis A. et al.** Preliminary computational approach of plasma dynamic evolution produced by low current table-top pinch plasma devices. *9th International Congress on Computational Mechanics (GRACM 2018), Chania, Greece.* 2018.
22. **Kaselouris E. et al.** Experimental and numerical study of the initial stages of explosion of thick single wire z-pinch. *41st EPS Conference on Plasma Physics.* VOL. 38F, P4.114, ISBN 2-914771-90-8), Berlin, 2014.
23. **Kaselouris E. et al.** The influence of the solid to plasma phase transition on the generation of plasma instabilities. *nature communications.* 2017, Vol. 8, 1713.
24. **Hassan Syed Murtaza Ph.D.** *Development and Studies of Plasma EUV Sources for Lithography.* s.l.: Nanyang Technological University, 2010.

25. **Shengtai Li. and Hui Li.** *Parallel AMR Code for Compressible MHD or HD Equations.* Los Alamos National Laboratory: s.n., 2006.

26. **Radiology Masterclass.** *Basics of X-ray Physics.* [Online] 2007. http://www.radiologymasterclass.co.uk/tutorials/physics/x-ray_physics_production#top_1st_img.

27. **Marc David Mitchell Ph.D.** *X-Pinch Plasma Dynamics Studied With High Temporal Resolution Diagnostics.* s.l.: Cornell University, 2007.

28. **Fitilis I. et al.** Diagnosing the initial stages from solid to plasma phase for dense plasma explosions. *Proceedings of Science (PoS) First EPs Conference on Plasma Diagnostics – 1st ECPD, Villa Mondragone, Frascati (Rome) Italy.* 2015.

29. **Sinars Daniel B. et al.** Plasma Imaging and Spectroscopy Diagnostics Developed on 100–500-kA Pulsed Power Devices. *IEEE VOL. 92, NO. 7.* 7 2004.

30. **Beg F. N. et al.** Table-top X-pinch for x-ray radiography. *Applied Physics Letters.* 2003, pp. 82, 4602.

31. **Chittenden J. P. et al.** Structural Evolution and Formation of High-Pressure Plasmas in X Pinches. *Physics Review Letters.* 2007, pp. 98, 025003.

32. **Gilbert Wilson Collins IV.** *STUDY OF X-PINCH DYNAMICS USING A LOW CURRENT (25KA) AND LONG-RISING (400NS) PULSE.* San Diego : San Diego State University, 2013.

33. **Wong Darren Jon Sien.** Studies on a plasma soft X-ray source for microlithography using a chemically-amplified resist. *Thesis (Ph.D.) National Institute of Education, Nanyang Technological University.* 2005.

34. **A website on Electrical Engineering.** *Electrotechnik.* [Online] 9 2009. http://www.electrotechnik.net/2009/09/what-is-rogowskis-coil.html.

35. **Hamamatsu.** *Photomultiplier tube assembly H1949-51.* [Online] 2017. https://www.hamamatsu.com/jp/en/product/alpha/P/3002/H1949-51/index.html.

36. **Eljen Technology.** *FAST TIMING EJ-228, EJ-230.* [Online] 2016. http://www.eljentechnology.com/products/plastic-scintillators/ej-228-ej-230.

37. **Martin Hipp, Peter Reiterer.** *User Manual for IDEA 1.7 Software for Interferometrical Data Evaluation.* s.l.: Technische Universitat Graz, 2003.

38. **Ghiglia Dennis C. and Romero Louis A.** Robust two-dimensional weighted and unweighted phase unwrapping that uses fast transforms and iterative methods. *J. Opt. Soc. Am. A.* January 1994, pp. no. 1, 107–117.

39. **Hunt B R.** Matrix formulation of the reconstruction of phase values from phase differences. *Journal of the Optical Society of America.* 1979, pp. Vol. 69, Issue 3, pp. 393-399.

40. **Press W. H. et al.** Numerical Recipes in C, second ed. *Cambridge University Press.* 1995, pp. 14, 62, 63, 109, 112.